



science.sciencemag.org/cgi/content/full/science.aaz1487/DC1

Supplementary Materials for  
**Accelerating water dissociation in bipolar membranes and for electrocatalysis**

Sebastian Z. Oener\*, Marc J. Foster, Shannon W. Boettcher\*

\*Corresponding author. Email: szo@uoregon.edu (S.Z.O.); swb@uoregon.edu (S.W.B.)

Published 3 July 2020 on *Science* First Release  
DOI: 10.1126/science.aaz1487

**This PDF file includes:**

Materials and Methods  
Supplementary Text  
Figs. S1 to S36  
Tables S1 and S2  
References

## Materials and Methods

### Nanoparticle water dissociation (WD) catalysts

Co<sub>2</sub>O<sub>3</sub>, Co:FeO<sub>x</sub> and Co:NiO<sub>x</sub> nanoparticles were synthesized via a hydrothermal method. 2 mmol metal acetate hydrate was dissolved in a mixture of 14 mL ethanol (98%) and 1.2 mL ultrapure water with vigorous stirring and sonication. For Co:FeO<sub>x</sub> and Co:NiO<sub>x</sub>, a 1:1 molar ratio of iron acetate to cobalt acetate or nickel acetate to cobalt acetate, respectively, was used. 2.5 mL of 25% aq. ammonia was added to the solution and the precursor solution was stirred until all residual metal acetate hydrate dissolved. Subsequently, the solution was transferred into a 45 mL Parr bomb, sealed, and then heated at 150 °C for 3 h. The synthesized nanoparticles were centrifuged and washed with water three times and ethanol one time. Afterwards, the dispersions were dried at 80 °C until all the solvent evaporated. All other nanoparticles were purchased from commercial sources as indicated in Table S2.

### Atomic-layer deposition (ALD) of TiO<sub>2</sub>

Nanoparticle powder (~200 mg) was distributed over flat, dish-shaped aluminum foil (~ 4 cm × 4 cm) creating a homogenous nanoparticle layer. The aluminum dish was then covered with a fine steel screen to prevent substantial quantities of particles from being carried away by the precursor and N<sub>2</sub> flows during the ALD process (Savannah S100, Ultratech). Another metal mesh with a larger metal grid was bent and placed onto the covered aluminum dish in such a way that the lid of the ALD chamber pushed the additional metal mesh down and ensured the fine mesh was held rigidly in place during the ALD process. The growth temperature of the chamber was set to 250 °C. The pulse times were set to 0.05 s for the water precursor and 0.5 s for Ti(NMe<sub>2</sub>)<sub>4</sub> (TDMAT) with N<sub>2</sub> purge times of 60 s after each step to ensure full removal of the precursors from the nanoparticle powders after each pulse. After the ALD process, the nanoparticle powders were transferred into glass vials.

### Membranes and ionomers

The cation-exchange membrane, Nafion® 212, was purchased from the Fuel Cell Store. The as-received membrane sheets were cut into ~ 4 × 4 cm<sup>2</sup> pieces and soaked in deionized water for at least 24 h. Nafion® D520 dispersion (5 wt % in ethanol) was used as ionomer for the cathode preparation (below). The anion-exchange membrane Sustainion® X37-50 was purchased from Dioxide Materials. The as-received membranes were cut into ~ 4 × 4 cm<sup>2</sup> pieces and soaked in 1 M KOH for 24 h, after which the membranes were rinsed and immersed again into a fresh 1 M KOH solution for another 24 h to complete the ion-exchange. Prior to the BPM assembly, the membranes were rinsed in copious amounts of deionized water. The compatible AEL ionomer, Sustainion® XA-9 (5 wt % in ethanol) was used for the anode preparation (see below).

### Anode and cathode catalyst dispersions.

100 mg of catalyst powder were dispersed in a mixture of 0.5 g H<sub>2</sub>O, 1.7 g isopropyl alcohol and 100 mg ionomer solution. For the cathodes, Pt black and Nafion® D520, and for the anode, IrO<sub>2</sub> and Sustainion® XA-9, were used. The dispersions were sonicated for at least 30 min or until all the nanoparticles were fully dispersed.

### Anode and cathode preparation

For the cathodes, 2 × 2 cm<sup>2</sup> pieces of Toray paper 090 (Fuel Cell Store) and for the anodes, 4 cm<sup>2</sup> sintered Ti frits electroplated with 1 μm Pt (purchased from Yinggao Metal Materials Co., Baoji, Shaanxi province, China) were used as gas-diffusion layers (GDLs). Pt black and IrO<sub>2</sub> (5-10 nm particle size, Fuel Cell Store) were used as cathode and anode catalyst, respectively, for all measurements. Before spray coating the catalyst/ionomer dispersion on a hotplate at 80 °C, the weight of the GDL substrate was recorded. The spray coating was stopped after the loading reached 2 mg cm<sup>-2</sup>. To improve the interface of the anode with the AEL and the cathode with the CEL, a thin layer of Sustainion® XA9 (1-2 wt% in ethanol) and Nafion® D520 (5 wt% in ethanol), respectively, were sprayed on top of the catalyst-coated GDLs until the weight reached 10 % of the total dry catalyst-ionomer loading (i.e. 0.2 mg cm<sup>-2</sup>). The anodes were then soaked in 1 M KOH for at least 1 h to fully ion-exchange the ionomer. The cathodes were used as prepared.

### Preparation of single and bilayer WD catalysts

Nafion pieces 4 × 4 cm<sup>2</sup> were placed flat onto a glass dish and residual water drops on the surface carefully removed with a clean laboratory tissue. The membranes were then fixed with tape to prevent wrinkling during the subsequent spray coating of the WD catalyst nanoparticles at 100 °C inside a fume hood. The exposed surface area (subtracting the taped edges) of the Nafion® pieces was ~ 10 cm<sup>2</sup>.

For the WD catalyst dispersions, 0.5 g of water, 1.7 g of isopropyl alcohol, and a fixed amount of catalyst powder were sonicated for at least 1 h to ensure good dispersion. The mass of WD catalyst added to the dispersion was calculated, taking into consideration the density of the material, the target thickness (~200 nm unless otherwise noted), the Nafion® surface area (~ 10

cm<sup>2</sup>), and the material loss during the spray-coating process. To determine the fraction of material lost during spray deposition, five ~ 10 cm<sup>2</sup> Si-wafer pieces (with the same size as the target area of the Nafion<sup>®</sup> membranes) were used as substrates. The Si was weighed, a known amount of catalyst powder was spray coated onto the substrates (at 100 °C), and the weight was recorded again. During those reference measurements, the spray coating gun was held at the same distance and angle from the substrate as during the actual sample preparation. Afterwards the mass loss per slide was averaged over the five substrates and determined to be ~ 90%. To prepare the bilayer WD catalysts, a different second nanoparticle layer was spray coated onto the first. For the second layer, ~14 mg XA9 ionomer solution was sometimes added to the catalyst mixture to aid dispersion, in particular for the noble-metal catalysts, while no effect on the WD kinetics was found for metal oxides that already dispersed well without ionomer. During all WD-catalyst spray-coating steps, the distance of the spray-coating gun to the substrate was held constant (~20 cm). Membranes with defects after WD catalyst coating (such as wrinkling) were rejected.

After the WD-catalyst spray coating, the tape at the edges of the Nafion<sup>®</sup> was removed inside the fume hood. To aid the removal of the Nafion<sup>®</sup>, and avoid exerting unnecessary force on the catalyst layers (e.g. via peeling of the Nafion<sup>®</sup>), water was carefully pipetted over the catalyst-coated membrane. The Nafion<sup>®</sup> absorbed the water and expanded which led to slow delamination from the glass dish. The catalyst-coated membrane was then placed with two tweezers into a water-filled glass dish to rehydrate.

#### Assembly of BPM MEAs

The electrodes and membranes were combined into a bipolar-membrane-electrode assembly (MEA), which was integrated into an electrolysis setup, and has been described in detail (33). First, the anode GDL with the IrO<sub>2</sub> catalyst layer and several gaskets were placed onto corrosion-resistant stainless-steel back plates containing serpentine flow channels (for the supply of ultrapure water and the transport of evolved O<sub>2</sub>). Then, the Sustainion<sup>®</sup> AEL was placed onto the catalyst-coated GDL and gaskets ensuring a wrinkle-free interface. Next, the Nafion<sup>®</sup> membrane with WD catalyst layers was carefully placed on top of the AEL with the WD catalyst layers facing the AEL, again, such that no wrinkled area or other irregularities were formed. Then additional gaskets and the Pt catalyst-coated cathode GDL were placed on top of the stack. Finally, a graphite block with serpentine flow channels (for the removal of the produced H<sub>2</sub>) was placed on top. The whole electrolyzer assembly was tightened with screws that are equally spaced around the edge of the metal block by a torque wrench (6 Nm). This type of MEA assembly is standard in AEM and PEM electrolyzers as well as fuel-cell studies, but has not been used for BPM studies. The advantage of the MEA approach is that it provides excellent physical adhesion between all layers due to the constant pressure of the anode and cathode GDLs which themselves are supported and sandwiched between fully rigid graphite and stainless-steel plates. Importantly, it also allows operation of the BPM MEA without any soluble electrolyte in ultrapure water due to the direct contact between ionically conducting membranes and electrodes.

#### Electrolyzer measurements:

For the polarization curves, the power supply was stepped from 2.5 to 50 mA·cm<sup>-2</sup> in 2.5 mA·cm<sup>-2</sup> steps, while 18.2 MΩ·cm water at 50 °C and at 300 ml·min<sup>-1</sup> was supplied via the serpentine flow channels of the stainless-steel block. The voltmeter output (measured directly at the current-collector plates to avoid the series resistance in the cables from influencing the measurements) was recorded for 1 min at each current-density step. The last voltage value of each time interval was used to plot the polarization curves, e.g. in Fig. S10-S15. Fig. S24 and S31 show that a voltage plateau is reached after the first few seconds of each current density step for current densities > 5 mA·cm<sup>-2</sup> (for low-current-density behavior, see below), indicating a quasi-steady state and allowing for reliable comparison of polarization curves of different BPM electrolyzers at 20 mA·cm<sup>-2</sup>. The current density is held constant for 1 min before recording the final voltage value.

#### Determination of $\eta_{wd} = 0$ V baseline for electrolyzer and error estimates:

To determine the theoretical response of the BPM electrolyzer with  $\eta_{wd} = 0$  V, we compared the results of several BPMs made with a single IrO<sub>2</sub> WD catalyst layer between the electrolyzer (with the standard IrO<sub>2</sub> anode OER catalyst and Pt cathode HER catalyst) and custom-built H-cell setup at the same temperature (see below). From the average values and the spread of the individual polarization curves (Fig. S4-S6) we determined the error (one standard deviation) to be ~ 5 mV for the H-cell measurements and ~ 8 mV for the electrolyzer measurements. As a result, the final error in Fig. 2 and Fig. 3 is ~ ± 9 mV.

#### H-Cell measurements:

The electrostatic potential drop across the bipolar membrane junction can be measured directly by using two pH-insensitive reference electrodes (Ag/AgCl) in the two adjacent compartments filled with 1 M acid and 1 M base electrolyte (2), as discussed more fully in the theory section below. The concentration of Cl<sup>-</sup> ions (and hence their chemical potential) is constant in both reference electrodes and, as a result, the electrochemical potential difference (of electrons) between the two Ag/AgCl reference electrodes is determined only by the electric potential difference across the bipolar membrane. Because the acid and base are both kept at high concentrations similar to their concentrations in the membrane, the electrostatic (Donnan) potentials developed across the aq. 1 M KOH | AEL and aq. 1 M H<sub>2</sub>SO<sub>4</sub> | CEL interfaces are minimized and constant through the

measurement. We also measure each Ag/AgCl reference electrode relative to each other in the same acidic or basic electrode compartment prior to each BPM measurement and correct for small differences between the two reference electrodes in the final measurement.

The H-cell measurements reported here differ in one important way from those typically used. Here, the working and counter electrodes, Pt-coated sintered Ti that pass the current, are directly in contact with catalyst layer pressed against the BPM (Fig. S27). Because concentrated acid/base are used in the H-cell to contact each side of the BPM, and the currents/distances are small, the  $iR$  potential drop through the electrolyte that permeates the gas-diffusion and catalyst layers is negligible. Therefore, the pH-insensitive reference electrodes that sense the electrostatic potential of the electrolyte can be placed exterior to the porous Ti/Pt frit current collectors (Fig. S3) and the Ti/Pt frit can be physically compressed by the H-cell design to mimic the environment inside the BPM electrolyzer.

The measurements in the H-cell were started by applying a small bias between anode and cathode with deionized water in the adjacent compartments. Then 10 M aq. KOH and H<sub>2</sub>SO<sub>4</sub> were used to adjust the concentrations in the two compartments to the final 1 M base/acid concentrations. This procedure prevents acid and base recombination inside the BPM junction during the cell setup, which can lead to rapid water formation and swelling (“ballooning”) of the BPM junction (10). Here, by driving a current between anode and cathode, which are in direct contact with the membrane surfaces, the BPM starts to dissociate water first. Subsequently, the 1 M base and 1 M acid concentrations are established in the adjacent compartments, allowing direct sensing of the electrostatic potential drop inside the BPM junction *via* the two Ag/AgCl reference electrodes.

Because the H-cell uses soluble acid and base in the cathode and anode compartments, respectively, part of the ionic current might be carried by co-ions (i.e. K<sup>+</sup> and SO<sub>4</sub><sup>2-</sup> as opposed to H<sup>+</sup> and OH<sup>-</sup> for ideal permselectivity). To quantify crossover, we measured [K<sup>+</sup>] in the acidic compartment of the H-cell as a function of time for two current densities (0 and 20 mA·cm<sup>-2</sup>) with ICP-MS (Fig. S35). The [K<sup>+</sup>] increases slowly at open-circuit conditions. This is due to diffusion of K<sup>+</sup> from the KOH compartment to the H<sub>2</sub>SO<sub>4</sub> compartment due to the non-ideal permselectivity of the Sustainion AEL. Sulfate is also expected to transport through the Nafion to reach the anode compartment, but that process should be slower due to the large size of sulfate and small size of the water channels in Nafion. Although this open-circuit crossover current is small in absolute terms (~0.13 mA) it is sufficient to affect the equilibrium membrane potential measurement (resulting in equilibrium membrane potentials lower than the ideal ~810 – 830 mV, depending on temperature). We find that this effect also depends on the history and preconditioning of the membrane (compare Fig. S33 to Fig. S36). At 20 mA·cm<sup>-2</sup>, the [K<sup>+</sup>] in the acidic cathode compartment follows a similar trend at shorter times and then increases more-rapidly after ~ 20 min. This incubation period is likely due to the time it takes for K<sup>+</sup> to initially transit the AEL. Although the total K<sup>+</sup> crossover current increases to ~ 1 mA (using the larger rate between 30 – 60 min) it remains a small fraction of the total current of 80 mA (4 cm<sup>2</sup> membrane surface area and with an acidic cathode compartment volume of 80 ml). As a result, the WD current efficiency of these BPMs is > 98% at 20 mA·cm<sup>-2</sup> and would be expected to continue to increase at higher current density. The steady-state membrane potential at 20 mA·cm<sup>-2</sup> is thus a good measure of true WD overpotential.

#### Dynamic light scattering (DLS) for electrophoretic mobility

The point of zero charge was determined via electrophoretic mobility measurements by dynamic light scattering (Mobius, Wyatt Technology). The acquisition time was 30 s with a read interval of 1 s. The results were the average of 10 DLS acquisitions for each pH value. The voltage amplitude and the electric field frequency were 10 V and 10 Hz by default, respectively, but were adjusted to obtain a stable reading, depending on the pH. The Smoluchowski zeta-potential model was used. Before the measurements, the catalyst powders were dispersed at a low concentration (~ 10 mg catalyst/L) in water and the pH was adjusted by adding KOH to make basic dispersions and HCl to make acidic dispersions, while maintaining the same ionic strengths for all dispersions. Then, the dispersions were sonicated for ~5 min and immediately transferred to a cuvette and the measurement started. We found that the use of certain glass vials (e.g. borosilicate Kimble, 60910-C) strongly influenced some of the PZC measurements. Therefore, for all dispersions we used polytetrafluoroethylene (PTFE) vials. Each measurement (which included an average of > 10 DLS acquisitions) was repeated at least three times to ensure accurate determination of the PZC. From those repeated measurements the reproducibility of the PZC measurement was determined to be ~ ± 0.5 pH units. The results are shown in Fig. S16 and Table S2.

#### Electrodes for three-electrode measurements

The catalyst dispersions contained 20 mg catalyst, 0.5 mg water and 1.7 mg IPA and either 20 mg Sustainion® XA9 (5 wt%) or Nafion® D520 (5 wt%) for the measurements in base and acid, respectively. The dispersions were sonicated for at least 30 min until homogenous and well dispersed. Glass slides were covered via e-beam evaporation with 20 nm Ti and 50 nm Au or 20 nm Ti and 50 nm Pt for measurements in acid or base, respectively. Afterwards the glass slides were weighed, exposed to O<sub>2</sub> plasma for 5 min, placed onto a hotplate at 80 °C, and the dispersions spray coated onto the surface. The weight was recorded again and the spray coating continued until the loading reached ~ 0.3 mg·cm<sup>-2</sup>. Afterwards, some of the catalyst powder was removed at

the edges of the substrates and a wire soldered to the metal-coated glass. The wire was fed through a glass tube, which was then sealed with acid and base-stable epoxy (Loctite EA 9460 Hysol) which was dried at ~50 °C. The geometric surface area of each electrode was determined by optical imaging on a flat-bed scanner.

To estimate the error for the electrocatalytic activity measurements in Fig. 3 of the main manuscript, we first calculated the standard deviation ( $\sigma$ ) of the electrocatalytic overpotential at 10 A·g<sup>-1</sup> (which was taken as the average value between forward and reverse sweeps to correct for capacitive components to the current) for each catalyst based on the repeated measurements shown in figs S19-22. Then we calculated an average standard deviation  $\langle\sigma\rangle$  for each set of electrocatalysts measured in one condition (e.g. HER in base, OER in acid, etc.) and took the uncertainty to be 2· $\langle\sigma\rangle$ . In this way, we increase the number of data points used in the error estimation yet avoid measuring many CVs for each of the many electrocatalysts. For several HER catalysts that were tested in acid, we found similar performance, which we ascribe to HER overpotentials primarily due to mass transport.

#### Three-electrode measurements in 1.0 M acid and 1.0 M base

The electrodes were immersed in the electrolyte and, together with a Pt counter electrode and an Ag/AgCl reference electrode (in acid) or Hg/HgO reference electrode (in base), connected to a potentiostat (BioLogic SP200 or SP300). A spinning stir bar was placed close to the electrode surface to remove generated bubbles. The electrolyte was sparged with N<sub>2</sub> to remove dissolved O<sub>2</sub>. We sparged one cell's electrolyte with H<sub>2</sub> (Fig. S22F) to quantify the effect of the dissolved H<sub>2</sub> concentration on the overpotential determination. The effect was small for the current densities used for the correlation plots in Fig. 3. The cyclic voltammograms were collected by first performing two cycles at 50 mV·s<sup>-1</sup>, followed by an impedance measurement to estimate the uncompensated series resistance, and one final cycle at 2 mV·s<sup>-1</sup>, unless otherwise noted. The data is shown in Fig. S19-S23.

#### Inductively-coupled plasma mass spectrometry (ICP-MS)

Analysis of [K<sup>+</sup>] in the H<sub>2</sub>SO<sub>4</sub> compartment of the H-cell due to crossover was performed using inductively couple plasma mass spectrometry (ICP-MS). An iCAP™ Qs ICP-MS (Thermo Scientific) was used for offline analysis with an ASX-500 autosampler (Agilent). The ICP-MS was operated in the hot plasma mode with an Ar cooling gas rate of 14 L/min and auxiliary Ar gas flow of 0.8 L/min. Samples were introduced with a self-aspirating PFA 100 MicroFlow nebulizer (ESI, Omaha, USA), a cooled quartz spray chamber (2.7 °C), and a nebulizer Ar gas flow of 0.970 L min<sup>-1</sup>. Dwell time for analysis was set to 1000 ms per peak and 5 sweeps. Signals were recorded for <sup>39</sup>K and <sup>59</sup>Co, with Co serving as an internal standard.

New 15 mL disposable polypropylene centrifuge tubes (Corning) were used for all standards and samples. Multi-element standards were prepared at concentrations of 100, 500, and 1000 ppb gravimetrically by adding the appropriate quantity of stock solution directly to the Trace-metal-grade (Fisher Chemical) 1.0 M H<sub>2</sub>SO<sub>4</sub> samples. The Co<sup>2+</sup> (internal standard) was from an elemental standard (Aldrich Chemistry), and the K<sup>+</sup> was from 99.98% trace-metal-basis-grade potassium hydroxide (Fisher Scientific). Trace-metal-grade (Fisher Chemical) 1.0 M H<sub>2</sub>SO<sub>4</sub> was used for the blanks. ACS-grade (Fisher Chemical) 3% H<sub>2</sub>SO<sub>4</sub> was used for the system rinse solution.

### **Supplementary Text**

#### Water dissociation in different contexts

Any process in which water is used as a reactant must involve, by some mechanism, the dissociation of water. However, this process could vary substantially, and hence be controlled by different factors in different contexts (thermochemical, electrocatalytic, biological, etc.). Although the pathways and overall reaction thermodynamics will be different, the underlying fundamental processes may be connected. Our work illustrates how heterolytic water dissociation (WD), H<sub>2</sub>O → H<sup>+</sup> + OH<sup>-</sup>, is catalyzed on surfaces and how the WD activity correlates with electrocatalytic activity for reactions where the electrochemical step that involves WD is thought rate limiting (e.g. H<sub>2</sub>O + e<sup>-</sup> → H<sub>ads</sub> + OH<sup>-</sup> for HER in base).

The work by Markovic and coworkers, (34, 35) for example, conceptually treats the WD step as a preceding step prior to metal-hydride formation, when interpreting the improved activity of Pt for HER in alkaline conditions after decoration with a sub-monolayer of Ni(OH)<sub>2</sub>. Possible alternative hypotheses, however, have been presented (36-38). The underlying challenge is that it has not previously been possible to discriminate the kinetics of electron transfer from those of WD – historically the steps could only be studied in series. The BPM approach presented here overcomes this fundamental challenge. For the first time, we show explicitly that the HER electrocatalytic overpotential under alkaline conditions correlates directly with the heterolytic WD overpotential measured in the BPM under locally alkaline conditions (Fig. 3).

This result supports the hypothesis that the fundamental chemical process of WD provides the dominant reaction barrier, by an apparently similar pathway, for both situations. During WD in the alkaline local environment of the AEL surface, OH<sup>-</sup> are driven by the gradient in electrochemical potential of OH<sup>-</sup> into the AEL, while the H<sup>+</sup> are moved toward the CEL (see discussion below on

BPM function). Inside the junction, the  $H^+$  can recombine with the  $OH^-$  generated from WD at the acidic CEL surface. For the alkaline HER reaction,  $OH^-$  are transported into the alkaline electrolyte environment (again by a gradient in electrochemical potential), while the transient  $H^+$  are removed through surface reaction to form metal hydrides, with a surface coverage dependent on the current density. Thus, there are similarities between the WD process on the AEL surface and during the alkaline HER. Computational catalysis models and *operando* experiments are needed to provide a more-detailed and quantitative physical picture.

We next provide additional discussion of WD in the context of related equilibrium surface-science studies of dissociative water absorption. For example, typical experiments on metal-oxides involve dosing a clean surface with water under ultra-high vacuum (UHV) conditions, leading to dissociative adsorption. The density of surface  $OH_{ad}$  can be measured, in equilibrium with undissociated absorbed water on the surface and in the gas phase, via spectroscopic techniques. For example, Campbell, Norskov and coworkers studied the dissociative adsorption of water on NiO(111) by measuring the enthalpy of adsorption and performing DFT calculations to obtain mechanistic insight (56). This process can be represented as:  $H_2O + M-O + M^* \rightarrow M-OH + M-OH$ . In the BPM device, the presence of an electrochemical potential gradient in  $H^+$  and  $OH^-$  could cause the ionization and spatial separation of these surface species to generate free  $H^+$  and  $OH^-$  to regenerate the surface for further WD. This catalytic WD mechanism (see description in section below), however, is different than the proton-transfer mechanism we propose for WD on oxides, which involves fully hydroxylated oxide surfaces and a two-step mechanism where  $H^+$  and  $OH^-$  are released in subsequent steps. No open metal sites for absorbing OH are invoked in the proton-transfer mechanism as they seem unlikely to exist in substantial concentrations in aqueous conditions for metal-oxide surfaces. We cannot, however, definitely prove one mechanism over the other. We speculate that the proton-transfer mechanism is more relevant for metal-oxide surfaces while the second mechanism involving hydroxylation of free metal sites may play an important role on more-inert (less-oxophilic), noble-metal surfaces, such as the ones present on the precious-metal HER catalysts. In addition to surface-speciation studies performed by dosing pure water, Winter and coworkers used liquid jet photoelectron spectroscopy to obtain information of oxide surfaces, resulting from pH-dependent water adsorption (57). As these studies are also typically performed at equilibrium, however, it is difficult to predict or directly compare to WD activities measured in the BPM without additional computation to connect the microscopic physical processes between the two environments/systems.

The basic working principles of BPMs: Theory and simulation

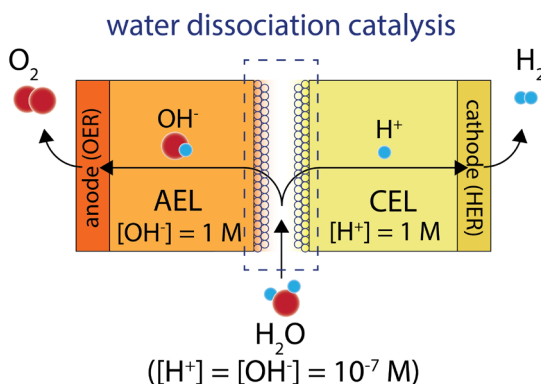


**Fig. S1.** A BPM electrolyzer drives the OER reaction in locally basic conditions and the HER in locally acidic conditions. Water is dissociated inside the junction, spatially separated from the HER and OER. The WD kinetics can therefore be studied independently from the reactions at the electrodes (which involve multiple electron transfers in series). The WD reaction maintains the acid and base concentration in the CEL and AEL, respectively, under continuous operation.

In this section, we discuss numerical simulation and analytical thermodynamic expressions from physical electrochemistry to describe the function of a BPM, as schematically depicted in Fig. S1. For simplicity, it helps to consider that the ionic BPM junction is similar to a semiconductor *pn* junction. Under equilibrium (no current flow) an electrostatic potential develops across the BPM that compensates for the different proton activities in the AEL and CEL, i.e. the chemical potential difference between the two phases. One can use two pH-independent reference electrodes (e.g. Ag/AgCl) to measure this electrostatic potential difference, which is ideally 0.83 V at 25 °C when the membranes are ~ 1 M in  $OH^-$  and  $H^+$ , respectively (see above for details of H-cell measurements). When current is passed through the system (for example by driving faradaic reactions on two electrodes separate from the reference electrodes), the electrostatic potential across the bipolar membrane changes, because additional driving force is needed to dissociate water and separate the incipient  $H^+$  and  $OH^-$  at the AEL/CEL junction. As we show below, this measured electrostatic potential change is precisely the water dissociation overpotential ( $\eta_{wd}$ ) and the required driving force for the WD reaction maintaining the constant  $[H^+]$  and  $[OH^-]$  within the CEL and AEL, respectively, at steady state.

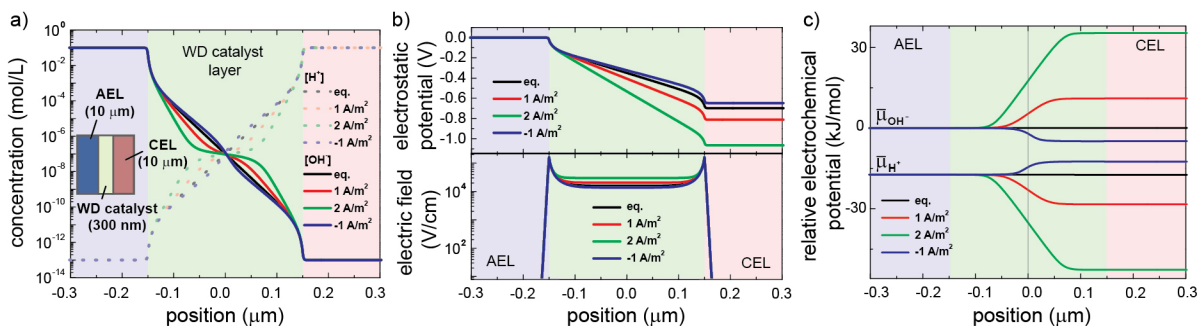


**Fig. S2.** Steady-state numerical simulations of a bipolar membrane consisting of an AEL and CEL (0.1 M free ions) sandwiching a WD catalyst layer. WD rate constants are independent of the local pH to minimize adjustable parameters in the model. (a) Concentration profiles of H<sup>+</sup> and OH<sup>-</sup> as a function of position,  $x$ , for different currents. Positive current represents driving WD in the junction and negative current represents driving H<sup>+</sup> and OH<sup>-</sup> recombination. (b) Electrostatic potential across the membrane (top), and electric field profile (bottom). The electrostatic potential drops essentially only across the catalyst layer due to the high conductivity of the mobile ions in the CEL and AEL. The equilibrium potential of  $\sim 700$  mV matches analytic theory given a  $\Delta\text{pH} = 12$  at 20 °C. (c) Electrochemical potentials, arbitrarily shifted for convenience. Changes in electrochemical potentials under current flow can be directly interpreted as the source of the WD overpotential,  $\eta_{\text{wd}}$ . Because species flow to lower electrochemical potential, H<sup>+</sup> is transported into the CEL and OH<sup>-</sup> is transported into the AEL with positive current as defined here. Water transport is assumed to be fast relative to its consumption in the catalyst layer at the experimental and simulated current densities and is thus not included in the model. The current densities explored in this initial model were limited by facile convergence of the simulation (for reference,  $1 \text{ A}\cdot\text{m}^{-2} = 0.1 \text{ mA}\cdot\text{cm}^{-2}$ ).

Simulations were performed in COMSOL Multiphysics (V. 4.4) using the transport of dilute species and electrostatics modules, building on earlier numerical simulations of BPMs (58). COMSOL solves the continuity equations together with Poisson's equation and the drift-diffusion equations under a prescribed flux boundary condition that defines the current. Generation and recombination of H<sup>+</sup> and OH<sup>-</sup> are modelled by the rate equations below. The BPM was finely meshed (0.1 nm) near the membrane interfaces where concentrations and potentials change sharply with position. Co-ions (e.g. K<sup>+</sup> and SO<sub>4</sub><sup>2-</sup>) are not included in the simulation for simplicity, and to match the experimental pure-water BPM electrolyzer setup where no soluble electrolyte is introduced. The specific values taken for the parameters were selected for experimental relevance, while also facilitating convergence of the simulation, which was found to be more difficult at higher concentrations and current densities. The CEL and AEL are modelled with a fixed anionic and cationic charge density, respectively, of 0.1 M. Diffusion coefficients of all ions are approximated to be  $10^{-9} \text{ m}^2 \text{ s}^{-1}$ . The relative permittivity of all hydrated phases (membranes, catalyst layer) are taken to be similar to that of liquid water,  $\sim 80$ . The kinetics of water dissociation and recombination are assumed to be different in the interfacial catalyst-containing region than in the free membranes. The WD chemical reaction is given by:



We define rate constants  $k_{f,i}$ ,  $k_{b,i}$ ,  $k_{f,\text{cat}}$ , and  $k_{b,\text{cat}}$ , where the subscripts differentiate between the forward and reverse processes as well as the different rates in the WD-catalyst region or for the intrinsic, uncatalyzed process. The rate constants  $k_{f,i}$  and  $k_{f,\text{cat}}$  are pseudo-zeroth-order rate constants with units  $\text{M}\cdot\text{s}^{-1}$  (i.e.  $[\text{H}_2\text{O}]$  is wrapped into the rate constant). The forward and reverse rate constants are related by detailed balance via the equilibrium constant,  $K_w = k_{f,i}/((c^0)^2 k_{b,i}) = k_{f,\text{cat}}/((c^0)^2 k_{b,\text{cat}}) = 10^{-14}$  at 25 °C. We note that the detailed mechanism of WD on the catalyst surface depends on the particular surface chemistry. The parameter  $k_{f,\text{cat}}$  represents a combined rate constant for the overall reaction consisting of several elementary steps (each having their own rate constant and intermediates) involving the catalyst surface. We also note that we model the system with one  $k_{f,\text{cat}}$  that represents the entire WD catalyst layer, while in reality the catalysts feature pH-dependent activity and different-activity WD catalysts can be used on the AEL and CEL surfaces. The parameter  $c^0$  is the standard-state concentration of 1 M, required to make the equilibrium constant unit-less. The values of  $k_{f,i}$  and  $k_{f,\text{cat}}$  are taken to be substantially different,  $10^{-4} \text{ M}\cdot\text{s}^{-1}$  and  $1 \text{ M}\cdot\text{s}^{-1}$ , such that the WD reaction occurs essentially exclusively in the catalyst region. The  $k_{b,i}$  and  $k_{b,\text{cat}}$  are calculated from  $K_w$ . The position-dependent rates of water dissociation ( $r_{\text{dis}}$ ) and H<sup>+</sup> and OH<sup>-</sup> recombination ( $r_{\text{rec}}$ ) in the catalyst layer are therefore taken as:

$$r_{\text{dis}} = k_{f,\text{cat}} \quad (2)$$

$$r_{\text{rec}} = \frac{(k_{f,\text{cat}}/K_w)[\text{H}^+][\text{OH}^-]}{(c^\circ)^2} \quad (3)$$

Water dissociation is forced in the membrane junction by setting appropriate flux boundary conditions for  $\text{H}^+$  and  $\text{OH}^-$  at the outside edge of the CEL and AEL, respectively. The simulation shows that the electrostatic potential drops essentially only across the catalyst layer, which is as expected due to the high concentration of mobile ions in the CEL and AEL. The equilibrium electrostatic potential of  $\sim 700$  mV across the membrane ( $\phi_{\text{BPM,eq}}$ ) matches analytic theory as described below.

The electrochemical potentials of  $\text{H}^+$  and  $\text{OH}^-$ ,  $\bar{\mu}_{\text{H}^+}$  and  $\bar{\mu}_{\text{OH}^-}$ , plotted in Fig. S2c, are given by:

$$\bar{\mu}_{\text{H}^+} = \mu_{\text{H}^+}^\circ + RT \ln a_{\text{H}^+} + F\phi \quad (4)$$

$$\bar{\mu}_{\text{OH}^-} = \mu_{\text{OH}^-}^\circ + RT \ln a_{\text{OH}^-} - F\phi \quad (5)$$

The terms  $\mu_{\text{H}^+}^\circ$  and  $\mu_{\text{OH}^-}^\circ$  are the standard chemical potentials, and  $a_{\text{H}^+}$  and  $a_{\text{OH}^-}$  the position-dependent activities. The term  $\phi$  is the position-dependent electrostatic potential referenced to an arbitrary zero point at the exterior of the AEL,  $F$  is the Faraday constant,  $R$  is the ideal gas constant, and  $T$  is the temperature (20 °C). By definition, the electrochemical potential of any given species is constant throughout the system at equilibrium, as reproduced by the simulations (Fig. S2c). We can thus set the equilibrium electrochemical potentials of  $\text{H}^+$  (or equivalently  $\text{OH}^-$ ) equal on both the AEL and CEL side of the BPM to obtain:

$$\phi_{\text{BPM,eq}} = \phi^{\text{CEL}} - \phi^{\text{AEL}} = \frac{RT}{F} \left( \ln \frac{a_{\text{H}^+}^{\text{AEL}}}{a_{\text{H}^+}^{\text{CEL}}} \right) \cong 0.058 \text{ V} \times \Delta\text{pH} \quad (6)$$

For the simulated system,  $\Delta\text{pH} = 12$ , and thus  $\phi_{\text{BPM,eq}}$  is predicted to be  $\sim 700$  mV. We emphasize that although  $\phi_{\text{BPM,eq}}$  is non-zero, the system is still at equilibrium as  $\bar{\mu}_{\text{H}^+}$  and  $\bar{\mu}_{\text{OH}^-}$  are independent of position. This is identical to the situation in a semiconductor  $pn$  junction where an electrostatic potential also exists across the junction at equilibrium. Mathematically, in both the BPM and  $pn$  junction the component of the free-energy change associated with the concentration gradient for each charged species is exactly canceled by the component associated with the electrostatic potential gradient. The physical source of the electrostatic potential is a thin space-charge layer that develops at the AEL and CEL junctions with the WD catalyst layer as the result of partial neutralization.

Experimentally, a current is passed through the BPM by driving HER and OER at the cathode and anode, placed at the edge of the CEL and AEL, respectively. This forces the system out of equilibrium to cause the dissociation of water and the flow of  $\text{H}^+$  and  $\text{OH}^-$  out of CEL and AEL, respectively. For positive currents in Figure S2a (representing water dissociation), this leads to depletion of both  $\text{H}^+$  and  $\text{OH}^-$  in the junction region. Because the concentrations of mobile  $\text{H}^+$  and  $\text{OH}^-$  are high in the bulk of the CEL and AEL, respectively, the chemical potential (e.g.  $\mu_{\text{OH}^-}^{\text{AEL}} = \mu_{\text{OH}^-}^\circ + RT \ln a_{\text{OH}^-}$ ) of those species remains constant as current flows through the BPM. The field,  $-\frac{d\phi}{dx}$ , is also negligible in the CEL and AEL regions due to the high conductivity of  $\text{H}^+$  and  $\text{OH}^-$ , respectively. Therefore, the gradients in  $\bar{\mu}_{\text{H}^+}$  and  $\bar{\mu}_{\text{OH}^-}$  shown in Figure S2c manifests themselves as a net change in electrostatic potential across the system,  $\phi_{\text{BPM}}$ , that drops entirely across the junction region between the two membranes (Figure S2b). These electrochemical potential gradients are responsible for separating  $\text{H}^+$  and  $\text{OH}^-$  as governed by the fundamental transport equation:

$$J_j(x) = - \left( \frac{C_j D_j}{RT} \right) \frac{d\bar{\mu}_j}{dx} \quad (7)$$

The variables  $J_j(x)$ ,  $C_j$ , and  $D_j$  are the flux, concentration, and diffusion coefficient of species  $j$ . As is evident from Figure S2c, the largest change in electrochemical potential with position occurs in the middle of the interfacial region where the concentrations of  $\text{H}^+$  and  $\text{OH}^-$  are small and thus  $\frac{d\bar{\mu}_j}{dx}$  must be large to drive the required ion currents.

We now use this framework to define the precise meaning of the WD overpotential,  $\eta_{\text{wd}}$ , and how it can be measured experimentally using the cell geometries described in the main manuscript. In traditional H-cell geometries, anode and cathode compartments are used to provide ionic contact the AEL and CEL, respectively. As discussed above, the equilibrium electrostatic potential across the membrane is governed by the fixed charge density in the AEL and CEL that determine the local pH and is  $\sim 0.83$  V when the concentrations of acid and base on either side of the membrane are  $\sim 1$  M at 25 °C. For an ideal bipolar membrane (i.e. without co-ion conduction such as  $\text{K}^+$  in the AEL and  $\text{SO}_4^{2-}$  in the CEL), this electrostatic potential is balanced by a concentration gradient in  $\text{H}^+$  because, at equilibrium,  $\bar{\mu}_{\text{H}^+}$  and  $\bar{\mu}_{\text{OH}^-}$  are constant throughout the system and thus no net ion current flows, as indicated by Eq. 6.

When current is driven through the BPM, for example by driving HER and OER on either side of the BPM,  $\bar{\mu}_{H^+}$  and  $\bar{\mu}_{OH^-}$  are no longer constant. The magnitude of the change in  $\bar{\mu}_{H^+}$  and  $\bar{\mu}_{OH^-}$  moving from the AEL to the CEL depends on the magnitude of the current flow (Figure S2c) and is the origin of  $\eta_{wd}$ . Because of the high concentration of  $H^+$  in the CEL and  $OH^-$  in the AEL, the ionic resistance of the ionomer regions is small and  $\frac{d\bar{\mu}_j}{dx}$  is negligible in the AEL and CEL (and likewise in the electrolyte compartments with strong base and acid). The electric field,  $-\frac{d\phi}{dx}$ , is also negligible in the AEL and CEL at low currents (e.g. less than  $\sim 10 \text{ mA}\cdot\text{cm}^{-2}$ ) due to the mobile ions, in analogy to, e.g., a metal that has mobile electrons.

The difference in  $\bar{\mu}_{H^+}$  (or equivalently  $\bar{\mu}_{OH^-}$ ) in the cathode compartment relative to the anode compartment under current flow is then given by:

$$\Delta\bar{\mu}_{H^+} = \bar{\mu}_{H^+}^c - \bar{\mu}_{H^+}^a = RT\ln a_{H^+}^c + F\phi^c - RT\ln a_{H^+}^a - F\phi^a \quad (8)$$

The superscript *c* and *a* represent the cathode and anode compartments. In the experiments here, 1.0 M acid and base are used to make near-ohmic ionic contact to the CEL and AEL, respectively. By roughly matching the activities of  $H^+$  and  $OH^-$  in solution and in the CEL and AEL, the electrostatic potential drop at interfaces between the AEL or CEL and the exterior electrolyte compartments are kept constant and small. As current is passed, the HER consumes  $H^+$  from the CEL and the OER consumes  $OH^-$  from the AEL. The pH difference is maintained by WD in the BPM junction and the flow of  $H^+$  into the CEL and  $OH^-$  into the AEL from the CEL/AEL junction. For an ideal BPM with no co-ion conduction,  $a_{H^+}^c$  and  $a_{H^+}^a$  are independent of current flow, consistent with Fig. S2a where the pH inside the AEL and CEL are independent of the current magnitude or direction. Because, by definition  $\Delta\bar{\mu}_{H^+,eq} = 0$  (and  $a_{H^+}^c$  and  $a_{H^+}^a$  don't change under current flow),  $\Delta\bar{\mu}_{H^+}$  is given precisely by  $\Delta\bar{\mu}_{H^+} = F(\phi_{BPM}(J) - \phi_{BPM,eq})$ , where  $\phi_{BPM}(J)$  is the electrostatic potential across the membrane with a net current density of *J*. The term  $\Delta\bar{\mu}_{OH^-}$  can be similarly defined and is identical in magnitude but opposite in sign. The terms  $\Delta\bar{\mu}_{H^+}/F$  and  $\Delta\bar{\mu}_{OH^-}/F$  are thus precisely the overpotentials driving WD and transport of the resulting ions through the junction region. Because the membranes are good ionic conductors, the WD catalyst layer is thin, and the current densities are relatively low ( $20 \text{ mA}\cdot\text{cm}^{-2}$ ),  $\Delta\bar{\mu}_{H^+}$  and  $\Delta\bar{\mu}_{OH^-}$  are dominated by free-energy losses in driving WD and separating the incipient  $H^+$  and  $OH^-$ .

We thus can measure  $\eta_{wd}$  through use of the two independent Ag/AgCl reference electrodes placed in nanoporous-glass-fritted tubes (Vycor) filled with saturated KCl. One reference is placed in the cathode compartment of 1.0 M aq.  $H_2SO_4$  and the other in the anode compartment with 1.0 M aq. KOH. The electrochemical potential of the electrons in the Ag wire,  $\bar{\mu}_{e^-}^{Ag}$  (i.e. which is the quantity measured by an external voltmeter), is set by the equilibria,  $AgCl + e^- \rightleftharpoons Ag + Cl^-$ . This leads to:

$$\bar{\mu}_{e^-}^{Ag} = \bar{\mu}_{Ag}^{Ag} + \bar{\mu}_{Cl^-}^s - \bar{\mu}_{AgCl}^{AgCl} \quad (9)$$

Where we take the notation that the subscript indicates the species of interest and the superscript the phase the species is in (*s* is the electrolyte solution). Because Ag and AgCl are pure, uncharged species, at unit activity, their electrochemical potential does not depend on the pH nor on the local electrostatic potential. Although  $a_{Cl^-}$  is the same in both reference electrodes,  $\bar{\mu}_{Cl^-}^s = \mu_{Cl^-}^o - RT\ln a_{Cl^-} - F\phi$ , *does* depend on the electrostatic potential difference across the BPM,  $\phi_{BPM}(J)$ . Therefore, the magnitude of the voltage measured across the two reference electrodes is given by:

$$\frac{|\bar{\mu}_{e^-}^{Ag,a} - \bar{\mu}_{e^-}^{Ag,c}|}{F} = \phi_{BPM}(J) \quad (10)$$

This analysis also assumes that any junction potentials across the Vycor porous glass frits separating the Ag/AgCl reference compartments from the anode/cathode compartments are negligible or, minimally, constant with applied current, which is a good assumption if concentrated electrolytes are present on both sides of the frit. Changes in the measured voltage from the ideal equilibrium value derived above ( $\sim 0.058 \text{ V} \times \Delta\text{pH}$  at  $20^\circ\text{C}$ ) can therefore be used directly to estimate  $\phi_{BPM}(J) - \phi_{BPM,eq} = \eta_{wd} = \left| \frac{\Delta\bar{\mu}_{H^+}}{F} \right| = \left| \frac{\Delta\bar{\mu}_{OH^-}}{F} \right|$  where the  $\Delta$  indicate the change in the value when moving across the BPM from one electrolyte compartment to the other under current flow.

#### Complications of conventional H-cell measurements

H-cell measurements of BPMs with acid and base in the adjacent compartments suffer from free acid and base transport into the BPM junction (enhanced by reduced ion-permeability of the membranes at high acid and base concentrations), thereby leading to significant water generation and sometimes blister formation (often called “ballooning”) inside the junction and possible dissolution of the WD catalysts (59). Therefore, often other neutral electrolytes such as NaCl,  $Na_2SO_4$ , or  $NaClO_4$  are used in both H-cell compartments (52). Under reverse bias, water is dissociated in the junction and the generated  $OH^-$  and  $H^+$  are transported

through the AEL and CEL, respectively, and into the salt solutions. However, because the activity (i.e. concentration) of OH<sup>-</sup> and H<sup>+</sup> are not controlled and change with time (and position), the thermodynamic potential for WD is not well defined. Often, significant current is observed before the “expected” onset BPM junction voltage of 0.83 V at 25 °C; this is a manifestation both of co-ion (e.g. Na<sup>+</sup>, Cl<sup>-</sup>) transport and the fact that the H<sup>+</sup> and OH<sup>-</sup> are not generated at unit activity. WD overpotentials estimated from such data assuming  $\phi_{\text{BPM,eq}} = 0.83$  V should be taken with caution as they underestimate the true WD overpotential measured relative to well-defined reference states. In principle, with neutral-pH solution on either side of the BPM, the equilibrium electrostatic potential drop across the BPM ( $\phi_{\text{BPM,eq}}$ ) should be zero, and therefore  $\eta_{\text{wd}} = \phi_{\text{BPM}}(J) - \phi_{\text{BPM,eq}} = \phi_{\text{BPM}}(J)$ . Nonetheless, the use of NaCl or other salts in BPM studies is justified from a practical point of view, i.e. if the application requires NaCl as electrolyte such as in electro dialysis.

The use of near-neutral solutions can lead to other issues in accurate measurement of  $\eta_{\text{wd}}$ . Based on the above analysis, taking  $\phi_{\text{BPM}}(J) - \phi_{\text{BPM,eq}} = \eta_{\text{wd}}$  requires that  $\mu_{\text{H}^+}^c$ ,  $\mu_{\text{H}^+}^a$ ,  $\mu_{\text{OH}^-}^c$ , and  $\mu_{\text{OH}^-}^a$  are all constant and independent of current magnitude (so that  $\eta_{\text{wd}}$  is manifested fully as an electrostatic potential and not as a change in the H<sup>+</sup> and OH<sup>-</sup> concentration difference across the two compartments which would not be sensed by the pH-independent Ag/AgCl electrodes). This is ensured in our approach by balancing H<sup>+</sup> and OH<sup>-</sup> transport into the cathode and anode compartments with consumption of OH<sup>-</sup> and H<sup>+</sup> by the electrode reactions in strongly acidic and basic electrolytes. However, in the presence of high Cl<sup>-</sup> concentrations, the Cl<sup>-</sup> oxidation reaction competes with OER, leading to, for example, the possibility of changing the pH in the anode compartment (as Cl<sup>-</sup> oxidation does not consume OH<sup>-</sup>). Furthermore, pH gradients could develop between the reference electrode and the membrane surface if mass transport is not sufficient in unbuffered salt solutions.

A final complication for traditional H-cell measurements arises from the lack of physical pressure on the membranes, which can lead to delamination of the membranes and catalyst layers under operation. Often more-elaborate fabrication methods are used, such as exerting prolonged pressure on the BPM at high temperatures to promote polymer binding or using various additional polymers inside the BPM junction (e.g. S-PEEK, see Table S1 for details), all of which can alter the BPM junction and make comparison of different WD catalyst systems challenging. It also limits the achievable thickness of the WD catalyst layer. The BPM electrolyzer and pressurized BPM H-cell configuration reported here solve these problems.

#### Control over catalyst location and local pH inside the BPM junction

One innovation in the work reported here is the ability to study WD catalysis in both acidic and basic local environments. By placing a stable nanoparticle layer such that it covers one membrane, e.g. the CEL, and systematically changing the WD catalyst on the other membrane’s surface, e.g. the AEL, we measure WD catalysis as a function of composition in a reasonably well-defined local-pH environment. The local pH will naturally depend on the distance from the membrane surface and the current density – the details of the H<sup>+</sup> and OH<sup>-</sup> concentration gradients requires additional numerical simulation coupled with *operando* experimental work to precisely determine.

Thickness-dependent measurements of single WD catalyst layers inside the BPM junction show that  $\eta_{\text{wd}}$  is minimized for a nominal thickness of ~100 - 200 nm (Fig. S8). For thicker WD catalyst layers, we hypothesize that ionic transport resistance across the WD catalyst layer increases the apparent overpotential. Fig. S9 shows SEM images of various nanoparticles covering the Nafion® surface with a nominal thickness of ~200 nm. The images show the majority of the surface is covered with WD catalyst. A cross-section clearly shows two distinct nanoparticle layers. This suggests that the WD catalyst contributing most is located near the membrane surface (i.e. full coverage is important) and below a thickness of ~ 100 nm.

The WD catalyst layers in the bilayer systems have a nominal thickness of ~ 200 nm each to prevent physical contact of the WD-catalyst top layer with the bottom membrane, and of the bottom WD-catalyst layer with the top membrane surface (see cross-section in Fig. S9). By comparing single-layer with double-layer BPM junctions, substantial effects on  $\eta_{\text{wd}}$  depending on the catalyst’s local pH are evident.

Fig. S4 shows the polarization curve for single-layer IrO<sub>2</sub> ( $\eta_{\text{wd}} \sim 50$  mV at 20 mA·cm<sup>-2</sup>) while Fig. 3a and Fig. S12 shows the effect of adding a NiO layer on the basic side ( $\eta_{\text{wd}} \sim 8$  mV for the bilayer system). Importantly, NiO likely dissolves if applied directly onto the CEL (consistent with known NiO dissolution in acid), leading to degraded BPM performance. Therefore, the effect of the NiO is not due to enhanced WD on the CEL surface (through possible penetration of the IrO<sub>2</sub> layer) but definitively due to enhanced WD on the AEL surface with NiO.

#### An alternative mechanism for water dissociation on surfaces

The related process of dissociative water adsorption on oxides has long been studied under ultra-high-vacuum conditions (31, 60). The reaction can occur via hydroxylation of free metal sites (M\*) and protonation of surface M-O species leading to two hydroxyl groups with different enthalpies of formation (43).



$M_a\text{-(OH)}^-$  is the more-acidic site, due to stronger M-O bonding, and  $M_b\text{-(OH)}^-$  the more-basic site (43). Within the BPM junction a gradient in the electrochemical potential of  $H^+$  and  $OH^-$  ( $\bar{\mu}_{H^+}$  and  $\bar{\mu}_{OH^-}$ ) drives transport and depletes  $H^+$  and  $OH^-$  from the WD region. Under these non-equilibrium conditions, free  $H^+$  and  $OH^-$  could be generated by the following reactions to complete an alternative catalytic cycle:



Because this mechanism (eq. 12-15) requires making/breaking M-O bonds, we hypothesize that, for oxides, it is slower than the proton-transfer mechanism presented in the main text. On less-oxophilic precious-metal alkaline HER catalysts (discussed in the main text), this WD mechanism (coupled with electron transfer) is more likely. To test these hypotheses, *operando* techniques to monitor non-equilibrium surface speciation combined with theory are needed.

### Effects of temperature

We perform electrolyzer and H-cell measurements to determine the  $\eta_{wd} = 0$  V baseline at 50 °C. H-cell measurements of BPMs are typically performed at 25 °C. With increasing temperature the equilibrium electrostatic potential across the BPM junction increases:

$$\phi_{BPM,eq} = \frac{RT}{F} \cdot \ln\left(\frac{a_{H^+}^{AEM}}{a_{H^+}^{CEM}}\right) = \frac{RT}{F} \cdot \ln(K_w(T)), \text{ for } a_{H^+}^{CEM} = a_{OH^-}^{AEM} = 1. \quad (14)$$

However, with increasing temperature  $\eta_{wd}$  is reduced due to the additional thermal energy increasing kinetics. This is evident in Fig. S18 which shows the results of a commercial Fumatech BPM and the IrO<sub>2</sub>-single-layer BPM measured at different temperatures. Because higher temperature increases the equilibrium potential but decreases  $\eta_{wd}$ , the measured membrane potential is similar for systems at 25 °C and 50 °C at current densities near 20 mA·cm<sup>-2</sup>, which is used as the reference point for the  $\eta_{wd}$  in Table S1. Even at 25 °C, the single-layer IrO<sub>2</sub> reference BPM outperforms a large set of commercial and research BPMs. The only possible exception is the 3d Al<sub>2</sub>O<sub>3</sub> BPMs fabricated by Pintauro and coworkers when measured with 0.5 M Na<sub>2</sub>SO<sub>4</sub> (11). However, as discussed above, the precise value of  $\eta_{wd}$  is difficult to discern at 20 mA·cm<sup>-2</sup> from those measurements due to the use of two neutral salt solutions on either side of the BPM. WD is not necessarily driven near standard-state conditions. When measured with 0.5 M KOH and 0.5 M H<sub>2</sub>SO<sub>4</sub> similar 3D-Al<sub>2</sub>O<sub>3</sub> BPMs exhibited  $\eta_{wd} \sim 60$  mV (24); the best BPMs reported here show  $\eta_{wd} \sim 8$  mV. At higher temperatures, the BPMs reported here improve at higher current densities >20 mA·cm<sup>-2</sup>. Given the above considerations, the performance comparison of the custom BPMs reported in our study to the various estimated literature values, as done in Table S1 at a current density of 20 mA·cm<sup>-2</sup>, seems reasonable.

### The role of the electric field in enhancing water dissociation

The role of the internal electric field across the BPM junction (Fig. S2) in enhancing the rate of WD has been an area of discussion (18, 24, 47, 48). If the intrinsic water dissociation rate constant is taken to be  $k_f = 10^{-3} \text{ M}\cdot\text{s}^{-1} = 10^{-6} \text{ mol}\cdot\text{cm}^{-3}\cdot\text{s}^{-1}$  (based on the recombination rate constant for  $H^+$  and  $OH^-$  measured to be  $\sim 10^{11} \text{ M}^{-1}\cdot\text{s}^{-1}$  and  $K_w = 10^{-14}$ ), the maximum intrinsic water dissociation current density ( $j_{wd}$ ) in the absence of any recombination is given by:

$$j_{wd} = Fk_f f_{H_2O} t \quad (15)$$

where  $F$  is the Faraday constant,  $f_{H_2O}$  is the fraction of the volume in the WD catalyst region filled by water (estimated to be 0.5, based on packing of catalyst particles), and  $t$  is the thickness of the interlayer region between the AEL and CEL where WD takes place (taken to be  $\sim 300$  nm; i.e. making the assumption that all the water in the interlayer catalyst region is identically active with the maximum intrinsic dissociation rate). The maximum  $j_{wd}$  is thus estimated to be  $\sim 1.5 \mu\text{A cm}^{-2}$  in our experimental configuration in the absence of chemical catalysis or electric-field effects. This is a factor of  $>10^5$  lower than the  $\sim 500 \text{ mA}\cdot\text{cm}^{-2}$  we observe experimentally in an electrolysis configuration with relatively small  $\eta_{wd}$ .

Both chemical catalysis and electric-field effects (i.e. the second Wien effect) have been proposed as mechanisms to speed up WD (24, 49). Our results are consistent with chemical catalysis of WD being the most-important effect. The model discussed, for example by Strathmann (49) and originally derived by Onsager (47), can be used to calculate the expected magnitude of the increased rate of WD due to an electric field (Eqs. 34 and 35 in Ref. (49) and Eq. 37 in Ref. (47)). As one example, consider SiO<sub>2</sub> or Al<sub>2</sub>O<sub>3</sub> nanoparticles as the WD catalyst layer. These are electric insulators with relatively small relative dielectric constants ( $\sim 4$  and  $\sim 9$ ) compared to water ( $\sim 80$ ). The thickness of the nanoparticle WD catalyst layer is  $\sim 300$  nm. Because both the AEL and CEL are good ionic conductors, any electrostatic potential drop will primarily occur across the nanoparticle WD catalyst layer (as also

manifested in the numerical simulation data included above). If one assumes the electrostatic potential drop is linear across the catalyst layer (which is reasonably accurate based on the simulation results for small current densities), one estimates that for an electrostatic potential drop of 1 V across 300 nm, the electric field is  $\sim 3 \times 10^6 \text{ V}\cdot\text{m}^{-1}$ . Based on Onsager's model this would enhance the rate of WD by a factor of only  $\sim 1.05$ , which is negligible compared to the  $>10^5$  rate increase observed experimentally. With a lower relative dielectric taken for water (which could be less mobile in the WD catalyst layer), for example  $\sim 10$ , the expected increase is a bit larger,  $\sim 1.4$ . As the electrostatic potential is increased from 1 V to 2 V, the rate of WD increases only by  $\sim 30\%$  with a relative dielectric of 10, which is small compared to the  $> 100$ -fold increase in WD current we observe experimentally with increasing  $\eta_{\text{wd}}$  a few hundred mV.

If the voltage drop is confined to a hypothetical 1-nm-thick region at the membrane surface (which is unrealistic for the geometries we study and the relevant depletion-region thicknesses) the junction electric field could be  $10^9 \text{ V}\cdot\text{m}^{-1}$ . The electric field enhancement is then predicted to be  $\sim 10^3$  (with relative dielectric  $\sim 80$ ) while the enhancement seen at  $500 \text{ mA}\cdot\text{cm}^{-2}$  is  $>10^7$  compared to the intrinsic WD current density ( $\sim 0.01 \mu\text{A}\cdot\text{cm}^{-2}$ ) if we assume the WD must occur over that 1-nm-thick region composed of pure water. The Onsager model thus supports the conclusion, based on our experimental data, that the electric-field enhancement to WD, if present, is a secondary effect compared to the chemical catalysis effect.

Recently, Yan et. al. used an equivalent circuit model to analyze the frequency and bias-dependent impedance response of a BPM (24). They extract apparent rate constants for WD which they find depend on the applied voltage and hence the current being passed through the BPM. They assign this dependence to an electric-field enhancement effect. However, as shown in the simulations above that used a field-independent rate constant  $k_{f,\text{cat}}$ , the WD current can also be increased under an applied bias by depletion of  $\text{H}^+$  and  $\text{OH}^-$  from the catalyst layer in between the AEL and CEL, thus reducing the recombination current and increasing the net rate of WD with the magnitude of the electric field. Distinguishing between these effects using an equivalent-circuit impedance model is challenging.

#### H-cell and electrolyzer measurements at low current densities

At low current density, H-cell measurements are substantially affected by leakage/transport of electrolyte ions across the BPM leading to a current that is unrelated to WD. As can be seen in Fig. S33, our BPMs are not different in that regard and show a lower open-circuit potential than expected for an ideal ion-selective BPM. At higher current densities this leakage current becomes negligible which, in part, motivates the choice of  $20 \text{ mA}\cdot\text{cm}^{-2}$  to report  $\eta_{\text{wd}}$  here and in the literature. The propensity for co-ion leakage is related to the ion selectivity of the alkaline and acidic membranes used. Ionomer optimization, beyond the scope of this work, could decrease co-ion transport. At  $20 \text{ mA}\cdot\text{cm}^{-2}$  we show co-ion transport is  $<2\%$  of the total ion current (Fig. S35).

Our electrolyzer measurements show current below 1.23 V of total applied voltage at small current densities of  $\sim 2.5 \text{ mA}\cdot\text{cm}^{-2}$  (see Fig. S29), which we tentatively ascribe to the consumption of free acid and base in the MEA. The AEL and CEL are pre-treated in strong base and acid (respectively) to obtain the fully  $\text{OH}^- / \text{H}^+$  forms of the ionomers. We rinse these membranes thoroughly (washing in copious amounts of pure water) to remove free acid and base, however, apparently a small amount remains. By consuming that free acid and base, HER and OER could be driven at the cathode and anode, respectively, at less than 1.23 V because WD is not required (free acid and base are consumed and the counter ions carry the current through the BPM). The behavior is transient and is reduced upon subsequent current sweeps (Fig. S33). The behavior is also apparent in the metal-oxide-free BPMs, and thus is not related to the WD catalyst. Because the work here focuses on much higher current densities ( $20 - 1000 \text{ mA}\cdot\text{cm}^{-2}$ ) where WD must occur to carry the current and reliable steady-state voltages are measured, this effect does not influence the interpretation of the results.

#### Influence of electrolyte ions on water dissociation

Given the correlation of WD activity with alkaline HER activity, any effect that has been reported to modulate alkaline HER activity may also be important in modulating WD activity. For example, co-adsorbed cations have been alternatively proposed to explain the changes in the HER overpotential with pH (36, 41, 42, 61). Ion-adsorption might also affect WD kinetics. In traditional H-cell measurements, the WD catalysts are exposed to electrolyte ions due to ion-crossover from the adjacent compartments, due to non-ideal membrane ion-selectivity. In the pure-water BPM electrolyzer we have no added soluble electrolyte, which eliminates any possible effect from counter ions (i.e. anything other than  $\text{H}^+$  and  $\text{OH}^-$ ). This may also contribute to the high performance we observe here, compared to literature reports, but more work is needed.

### Comparison to electro dialysis systems

The primary difference between the BPM measurements reported here, and those reported for electro dialysis systems in the literature, is the lack of salt solution for the measurements here in pure water. Even under operating conditions with high currents driving WD, some auxiliary salt ions will be present at the BPM junction during electro dialysis. These ions could adsorb to the WD catalyst surface as well as modulate the electric field distribution within the WD catalyst region. Future experiments are needed to understand the role of auxiliary electrolyte ions on the WD reaction which may help explain some of the findings in the electro dialysis community and further elucidate the link between WD inside the BPM and the WD reaction occurring during electro catalysis.

### Modes of degradation of BPM electrolyzer at high current densities

The inset in Fig. 4 shows that the total voltage of the BPM electrolyzer increases by 40 mV over a 4 h period when held at 500 mA·cm<sup>-2</sup>. There are a number of possible phenomena that might explain this degradation behavior which, for practical application at high current densities, must be mitigated.

For the stability test shown in Fig. 4 at 500 mA cm<sup>-2</sup>, we used an IrO<sub>2</sub>|NiO bilayer WD catalyst. Even though NiO is in contact to the alkaline AEM it is possible that a part of the NiO layer (particularly the one facing the IrO<sub>2</sub> layer on the CEM) is exposed to a non-alkaline pH that leads to slow dissolution of the material. To test this hypothesis, long-term studies with metal-oxide catalysts with varying stability in acid and base are needed. Post-mortem analysis of the spatial distribution of cations that might originate from the WD catalyst will also be useful.

The ionomer and membrane could also degrade due to insufficient water transport through the thick membranes (~50 μm each) and into the BPM junction where it is consumed. We observe a characteristic inflection point in the polarization curves at current densities above ~800 mA cm<sup>-2</sup>, which is often associated with degradation due to membrane dehydration (64). If the water transport through the membranes (and against the hydrated ion flow) cannot keep up with the WD, the concentration of water inside the junction decreases and thus the degree of hydration of hydroxide ions and protons decreases. Dehydrated hydroxide ions are strong nucleophiles that can degrade the membrane. It is likely that even at 500 mA cm<sup>-2</sup> junction dehydration is leading to slow degradation. To test this hypothesis, the water transport towards the junction can be systematically controlled, e.g. by thinning down either the CEL or the AEL (or both).

### Comparison of BPM and AEM electrolyzer performance

We hypothesize that the deviation of the BPM electrolyzer performance from that of the reference AEM electrolyzer is caused by water-transport limitations and the ionic series resistance in the WD catalyst layer. At current densities above 800 mA cm<sup>-2</sup>, we observe pronounced irreversible performance degradation for BPM electrolyzers which we ascribe to, as previously reported (64), water-transport limitations in BPMs (see Fig. S32). We hypothesize that water-transport limitations lead to voltage increases at lower current densities as well. This can be tested, and possibly mitigated, by thinning one of the ionomer layers to increase water transport rates.

The thickness of the individual WD catalyst layers (~200 nm) were chosen to limit the contact of each catalyst layer to only the AEL or CEL (and not both due to incomplete coverage), while also not causing a pronounced voltage increase due to ionic series resistance at 20 mA cm<sup>-2</sup> (see Fig. S8 and S9). At higher current densities, however, the voltage loss due to the ionic series resistance is likely significant. Therefore, a higher-performing BPM likely requires an overall thinner interfacial WD region, while maintaining full WD catalyst coverage on each membrane surface. Engineering the ionic conductivity of the WD catalyst layer may also be possible. Full optimization of the BPM junction performance for high-current-density operation will be guided by experimental studies coupled with multi-physics simulations that elucidate steady-state concentration gradients and the location of electrochemical potential gradients inside the BPM junction.

Supplementary Figures

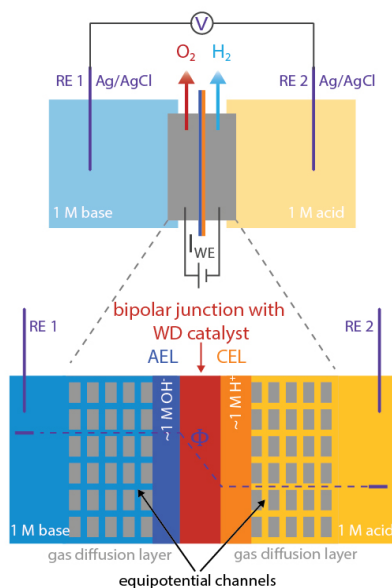


**Fig. S3. Equipotential channels in the MEA H-cell setup.** The custom-made H-cell (top) allows measuring the electrostatic potential drop across the BPM junction directly via two pH-insensitive Ag/AgCl electrodes. A central part of the custom-made H-cell are two rigid GDLs placed directly onto, and compressing, the self-made BPM. The GDLs ensure constant mechanical pressure preventing delamination of the different parts, a common issue encountered in BPMs. The placement of the GDLs onto the BPM does not prevent the accurate measurement of the electrostatic potential drop across the BPM junction (bottom). The respective electrolytes are directly in contact with the BPM via microscopic electrolyte channels in the GDLs and catalyst layers. The potential drops driving catalysis occur over the nm-thick Helmholtz layer at the catalyst surface. Because little current is carried through the electrolyte permeating the GDL, the microscopic electrolyte channels are essentially equipotential and allow sensing of the electrostatic potential at the membrane/electrolyte boundary.

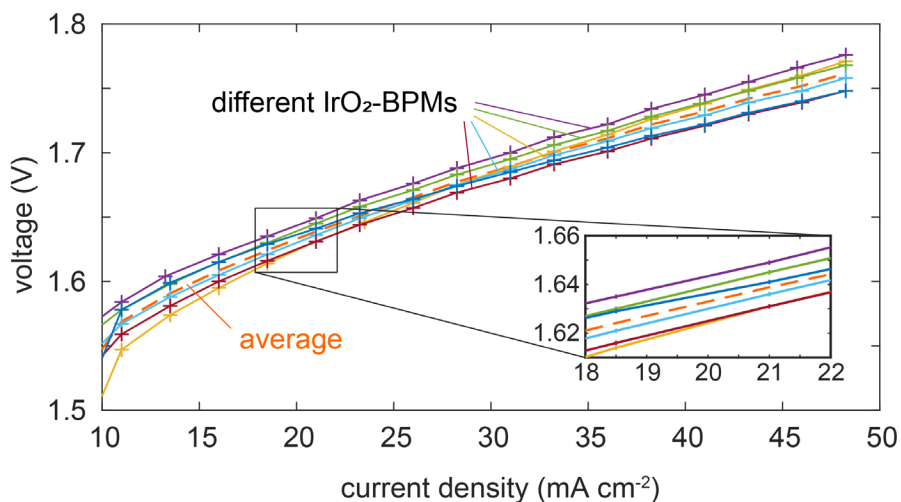


**Fig. S4. Multiple BPM electrolyzer polarization curves with single-layer IrO<sub>2</sub> WD catalyst and the average response, recorded at 50 °C.** An error of 8 mV (one standard deviation) at 20 mA·cm<sup>-2</sup> was determined. The voltage is the total applied voltage across the two-electrode electrolyzer stack and includes all transport and overpotential losses.

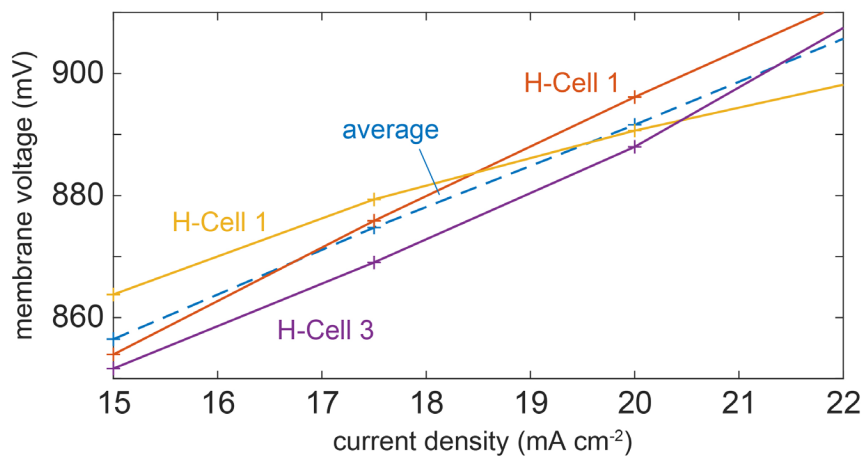


**Fig. S5. Multiple H-cell polarization curves of single-layer IrO<sub>2</sub> BPMs and their average, recorded at 20 °C.** An error of 5 mV (one standard deviation) at 20 mA·cm<sup>-2</sup> was determined. The H-cell measurements allow a more-direct determination of  $\eta_{wd}$ . The voltage recorded here is the electrostatic potential drop across the membrane recorded with the two Ag/AgCl reference electrodes placed in the electrolyte compartments (see SM discussion).

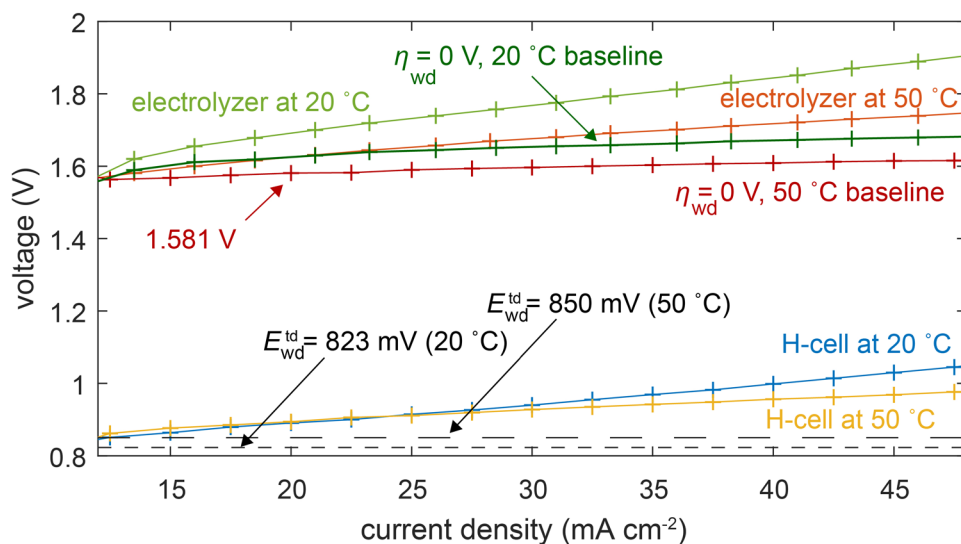


**Fig. S6. Determination of the theoretical  $\eta_{wd} = 0$  V baseline for electrolyzer measurements.** The  $\eta_{wd} = 0$  V baseline for the electrolyzer measurements was determined by comparing the electrolyzer results of single-layer IrO<sub>2</sub> BPMs (orange) to H-cell measurements of single-layer IrO<sub>2</sub> BPMs at 50 °C (yellow). The  $\eta_{wd} = 0$  V baseline (dark green) was obtained by subtracting  $\eta_{wd}$  in the H-cell measurement from the total voltage response of the BPM electrolyzer. For comparison, an H-cell measurement (blue) and electrolyzer (orange) at 20 °C are also shown.

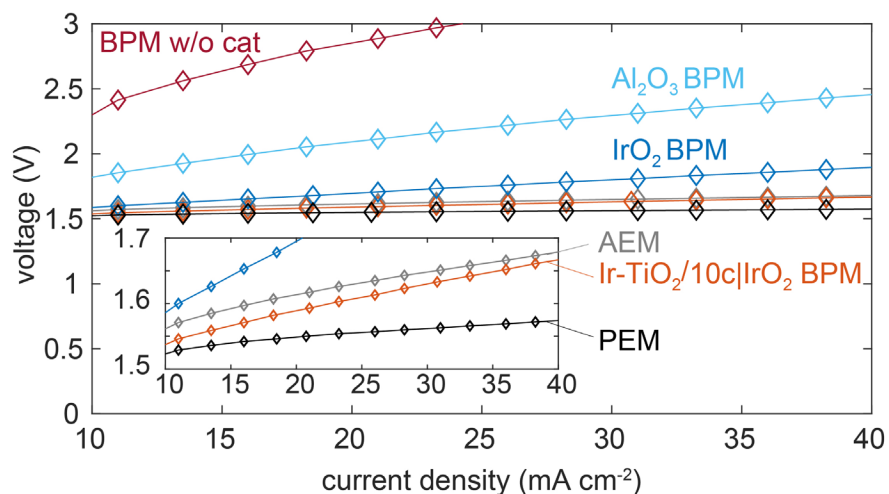


**Fig. S7. Comparison of BPM, AEM and PEM electrolyzers at low current densities.** For all measurements the same anode and cathode GDLs and catalysts are used. The reference AEM electrolyzer (gray) performs worse than the PEM electrolyzer (black), which can be ascribed to the superior performance of the Nafion<sup>®</sup> membrane and ionomer over the Sustainion<sup>®</sup>, and the higher activity of IrO<sub>2</sub> and Pt as HER and OER catalysts, respectively, in acid versus base. One of the best-performing double-layer BPMs (orange), which also contains the Sustainion<sup>®</sup> AEL on the anode-facing side, outperforms the AEM electrolyzer at low current densities. Figure 4 in the main manuscript shows the electrolyzer performance for larger current density after stabilization. This is direct proof that  $\eta_{wd}$  is small under these conditions. Without an extra WD catalyst layer (red) the BPM performs substantially worse, because WD is likely only catalyzed by the membrane end groups (i.e. on the AEL side). Al<sub>2</sub>O<sub>3</sub>, which is often used in the literature as standard WD catalyst, performs poorly (bright blue) compared to other WD catalysts such as the IrO<sub>2</sub> (dark blue) and the high-performance bilayer systems.

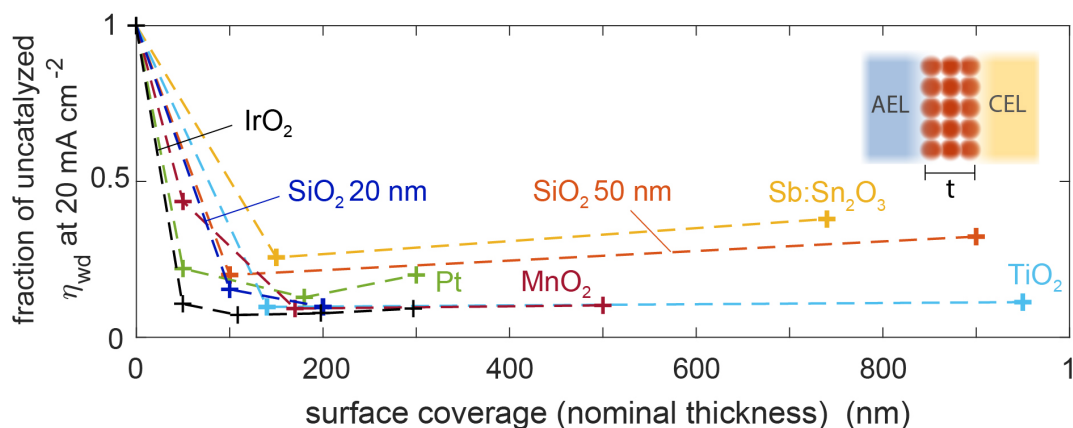


**Fig. S8. Thickness/coverage-dependence of single-composition WD catalyst layers.** All catalysts show a substantial reduction in  $\eta_{wd}$  after the first ~100 - 200 nm of nanoparticle catalyst layer is added. Further loading tends to decrease performance. These results, together with the SEM images in Fig. S9, indicate catalytic WD that is confined to a region near the membrane surface at 20 mA·cm<sup>-2</sup>. At larger junction thickness, a performance loss from series resistance through the WD catalyst layer (that is likely to have a high ionic resistance) is hypothesized. The overpotential is plotted as a fraction of the uncatalyzed BPM,  $\eta_{wd} = 1.95$  V at 20 mA·cm<sup>-2</sup>.

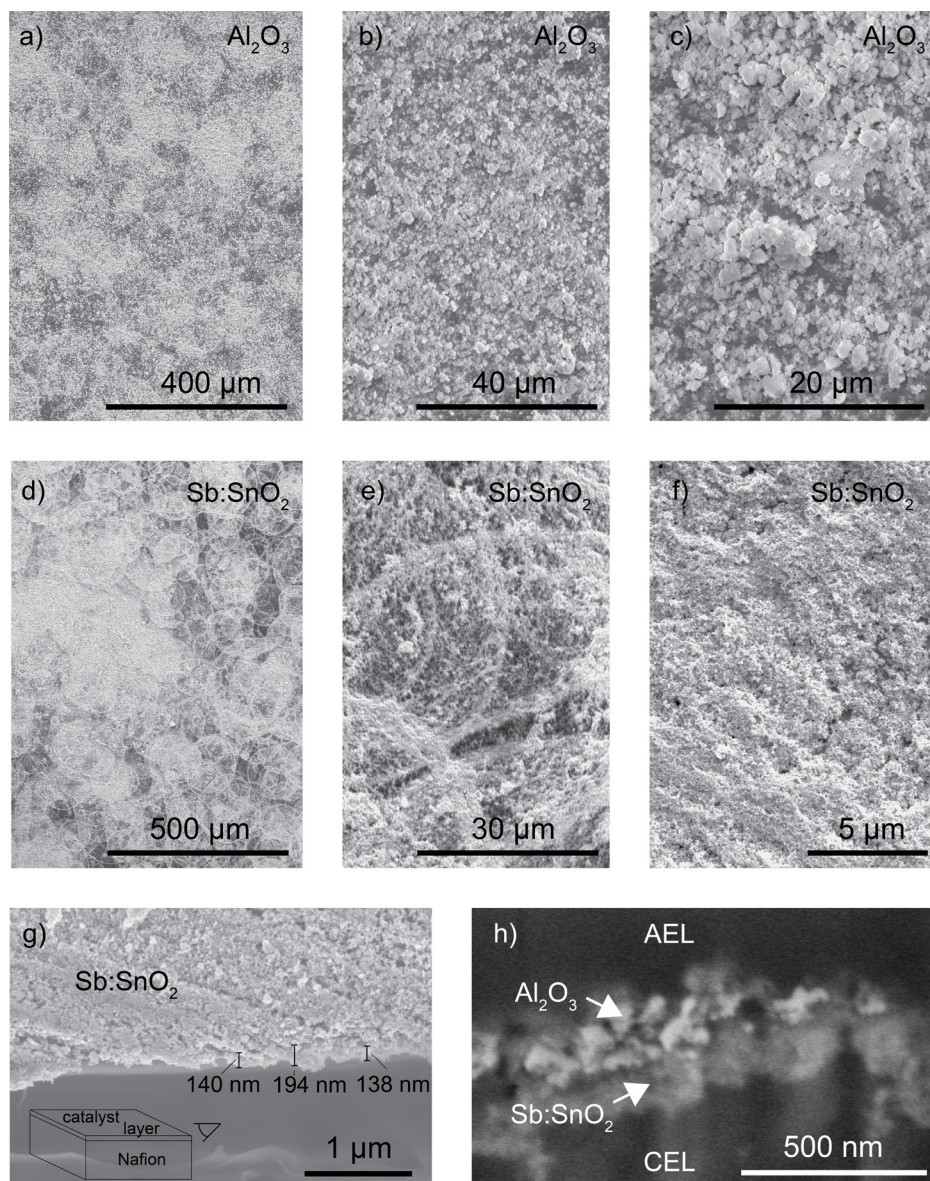


**Fig. S9. Top-down SEM images of single  $\text{Al}_2\text{O}_3$  and  $\text{Sb}:\text{SnO}_2$  layer on Nafion and cross-section of  $\text{Al}_2\text{O}_3|\text{Sb}:\text{SnO}_2$  bilayer junction.** (a-f) The nanoparticle layers cover most of the Nafion<sup>®</sup> surface, while some smaller uncovered Nafion<sup>®</sup> patches are visible. With decreasing thicknesses ( $< 200$  nm) we also observe decreasing coverage. Critically, we also observe an effect of the location of the catalyst layers (i.e. next to the basic AEL or acidic CEL surface) on  $\eta_{\text{wd}}$ . Thus the first spray-coated nanoparticle film with a thickness of  $\sim 200$  nm (shown in the SEM images here) is able to block most of the Nafion<sup>®</sup> surface from the next catalyst layer which will be in contact with the AEL after the BPM MEA preparation. The nominal thickness dependence in Fig. S8 and the coverage shown here indicate that most of the catalytic activity stems from the regions close to the AEL and CEL surface. The observed apparent thickness dependence of  $\eta_{\text{wd}}$  may in fact be better described by a coverage dependence; more work is needed to differentiate between the two. (g-h) The cross-section, obtained *via* cryogenic focused-ion beam milling, shows an  $\text{Al}_2\text{O}_3|\text{Sb}:\text{SnO}_2$  bilayer junction. As can be seen, the total thickness of the nanoparticle layers is approximately 400 nm, with two apparent nanoparticle phases, each around 200 nm in thickness.

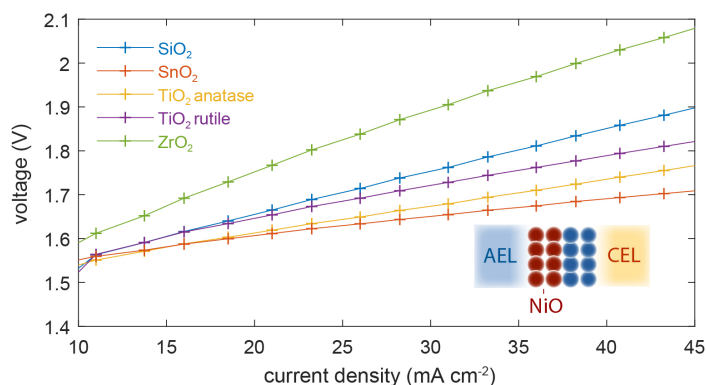


**Fig. S10. Electrolyzer polarization curves of WD-catalyst layers on the acidic CEL surface with a constant NiO layer on the basic AEL surface.** All measurements were performed at 50 °C and with pure-water feed using the standard anode (IrO<sub>2</sub>/Pt/Ti) and cathode (Pt/C) electrolyzer configuration. The voltage recorded is the total electrolysis voltage.

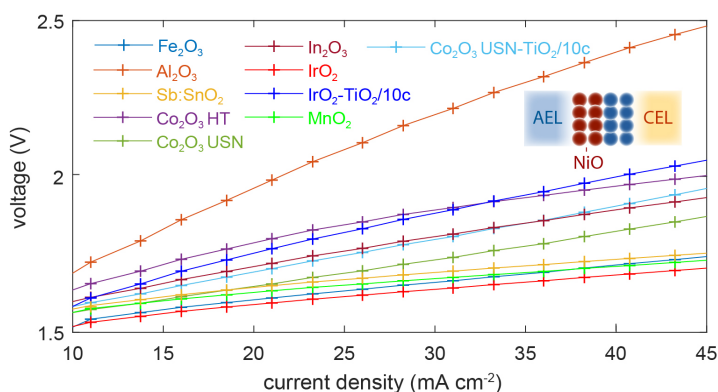


**Fig. S11. Electrolyzer polarization curves of WD-catalyst layers on the acidic CEL surface and a constant NiO layer on the basic AEL surface.** All measurements were performed at 50 °C and with pure-water feed using the standard anode (IrO<sub>2</sub>/Pt/Ti) and cathode (Pt/C) electrolyzer configuration. The voltage recorded is the total electrolysis voltage.

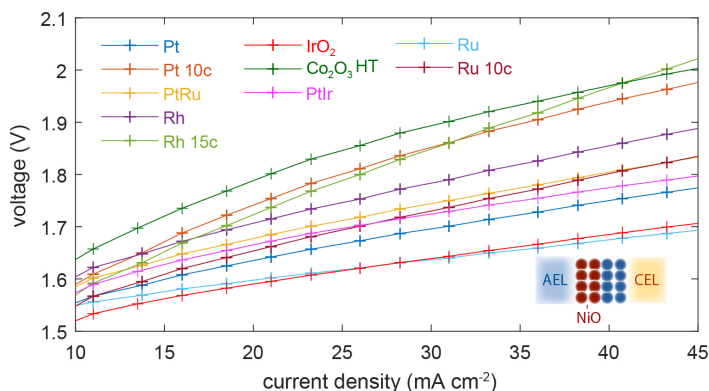


**Fig. S12. Electrolyzer polarization curves of various acid OER catalyst layers (tested here for WD activity) on the acidic CEL surface and a constant NiO layer on the basic AEL surface.** All measurements were performed at 50 °C and with pure-water feed using the standard anode (IrO<sub>2</sub>/Pt/Ti) and cathode (Pt/C) electrolyzer configuration. The voltage recorded is the total electrolysis voltage.

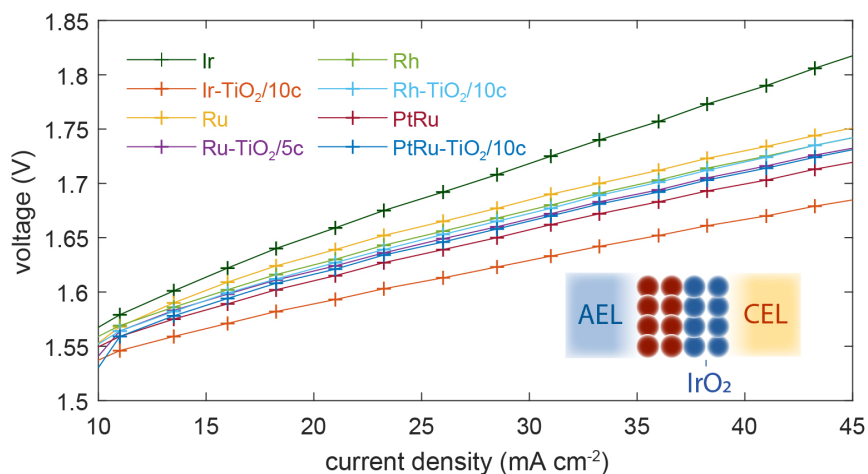


**Fig. S13.** Electrolyzer polarization curves of various base HER catalyst layers (tested here for WD activity) on the basic AEL surface and a constant IrO<sub>2</sub> layer on the acidic CEL surface. All measurements were performed at 50 °C and with pure-water feed using the standard anode (IrO<sub>2</sub>/Pt/Ti) and cathode (Pt/C) electrolyzer configuration. The voltage recorded is the total electrolysis voltage.

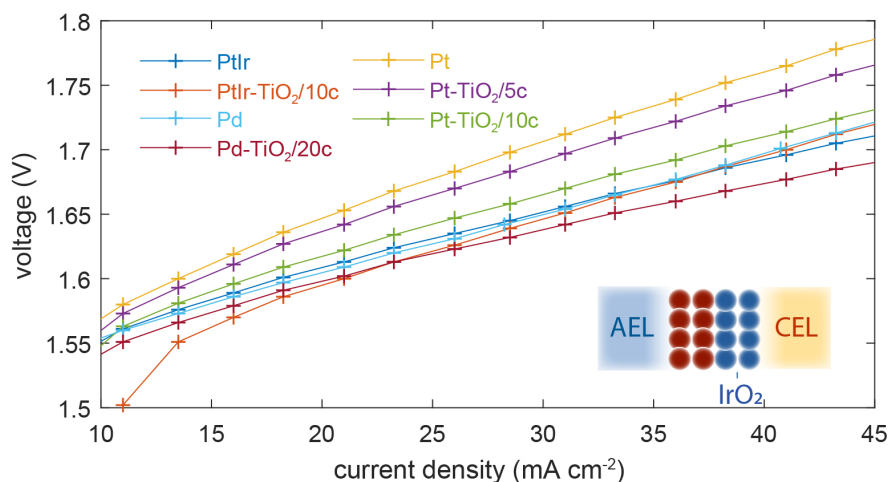


**Fig. S14.** Electrolyzer polarization curves of various base HER catalyst layers (tested here for WD activity) on the basic AEL surface and a constant IrO<sub>2</sub> layer on the acidic CEL surface. All measurements were performed at 50 °C and with pure-water feed using the standard anode (IrO<sub>2</sub>/Pt/Ti) and cathode (Pt/C) electrolyzer configuration. The voltage recorded is the total electrolysis voltage.

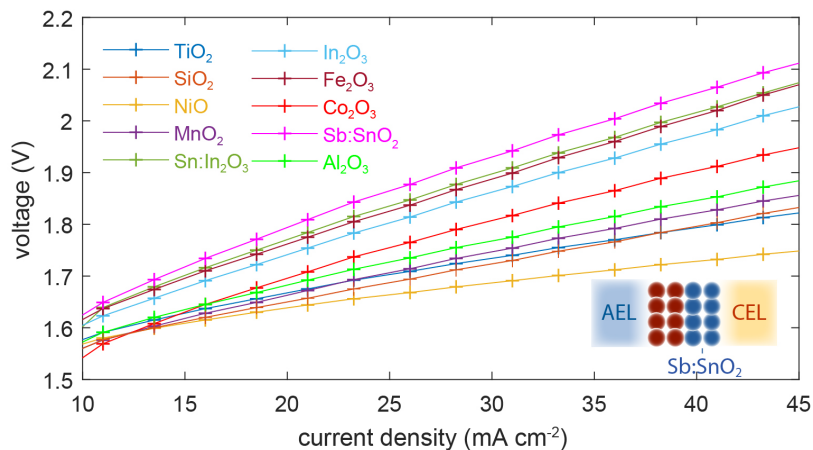


**Fig. S15. Electrolyzer polarization curves of different catalysts on the basic AEL surface and a constant Sb:SnO<sub>2</sub> layer on the acidic CEL surface.** All measurements were performed at 50 °C and with pure-water feed using the standard anode (IrO<sub>2</sub>/Pt/Ti) and cathode (Pt/C) electrolyzer configuration. The voltage recorded is the total electrolysis voltage.

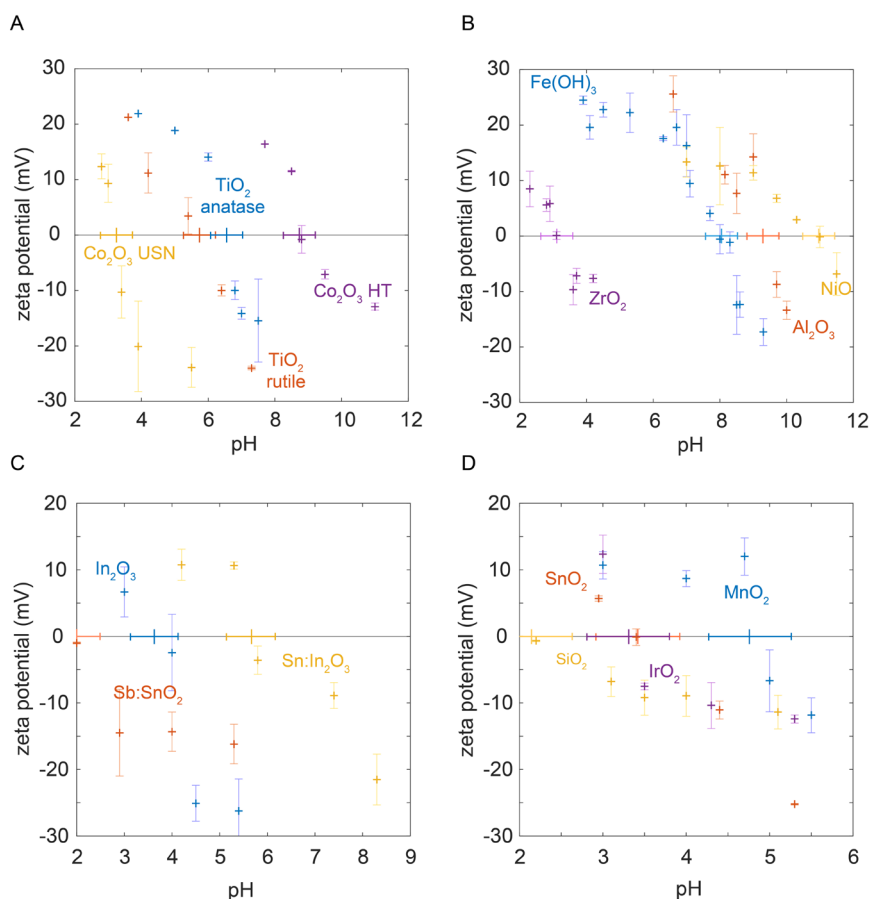


**Fig. S16. Determination of point of zero charge via electrophoretic mobility measurements and dynamic light scattering.** Most nanoparticle catalysts showed a PZC in the range of pH 2 - pH 12 ( $\pm 0.5$  pH units), with the exception of Sb:SnO<sub>2</sub>. For each catalyst, the measurements were repeated three times to ensure an accurate estimate of the PZC and the average is reported in the manuscript with the standard deviation of the values, rounded to the nearest 0.5 pH unit, is taken as the error. One representative set of measurements is shown here. See Methods for a detailed description of procedure.

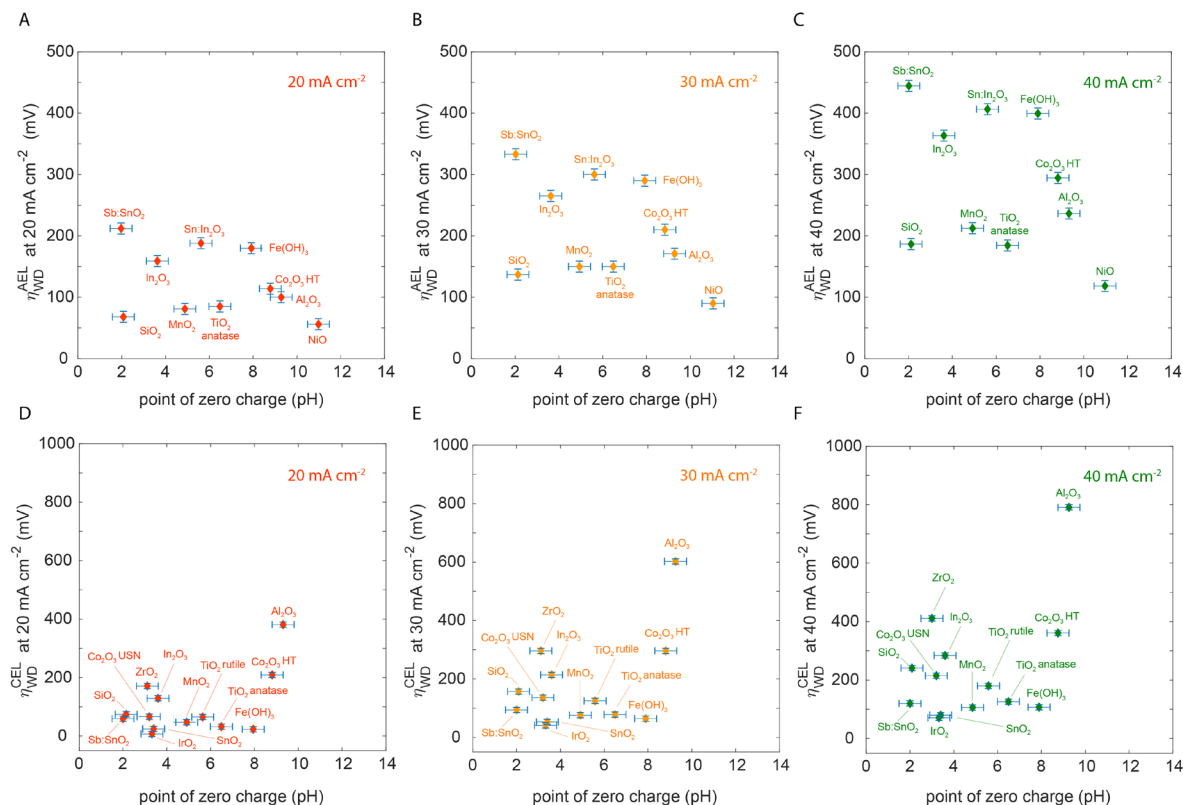


**Fig. S17. Correlation of WD overpotential with point of zero charge of Fig. 2 in the main text as a function of current density.** Increasing the current density maintains the observed trend, supporting the choice of the current-density range to study WD kinetics.

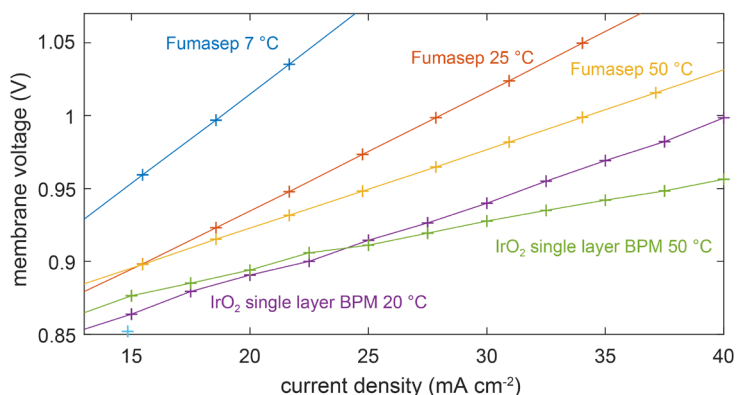


**Fig. S18. Temperature dependence of  $\eta_{wd}$  in H-cell measurements.** The influence of the temperature can be seen by comparing the performance of the commercial Fumasep BPM (Fumatech) and single-layer IrO<sub>2</sub> BPM at the temperatures indicated. At low current densities, both membranes show a voltage increase with temperature, while at higher current densities a substantial voltage reduction is apparent with increasing temperature. This is consistent with a model that treats WD inside the BPM as a catalytic reaction. When the temperature increases the open-circuit electrostatic potential across the membrane increases (see theory discussion above). The higher temperature increases the kinetics of WD and decreases the rate of voltage increase with increasing current.

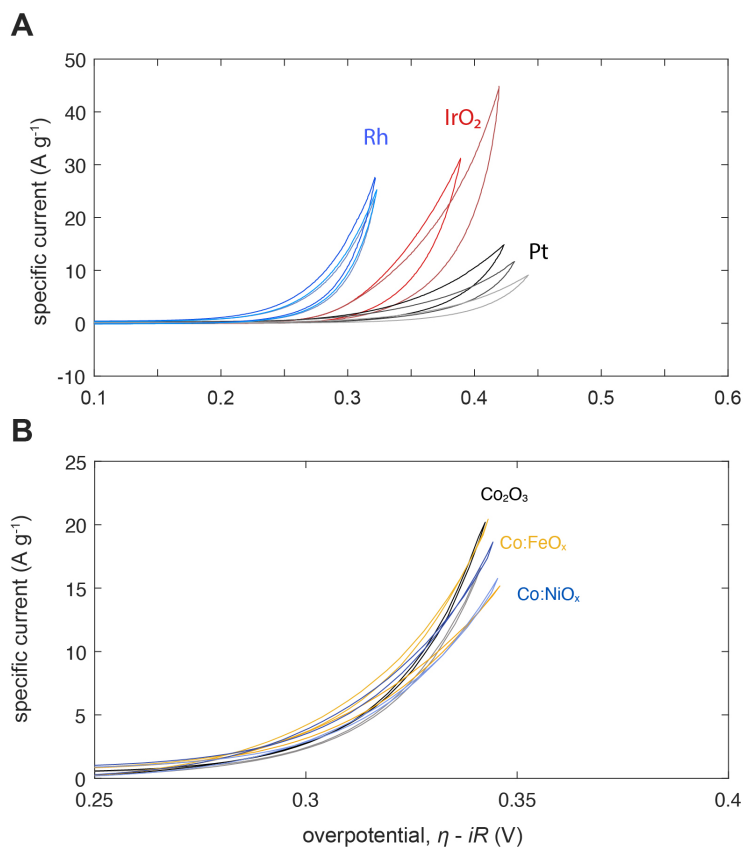


**Fig. S19. Cyclic voltammograms of OER catalysts in 1.0 M KOH.** The scan rate is 2 mV·s<sup>-1</sup>. The uncompensated  $iR$  drop was corrected for after data collection based on impedance measurements of uncompensated resistance, as indicated in the Methods.

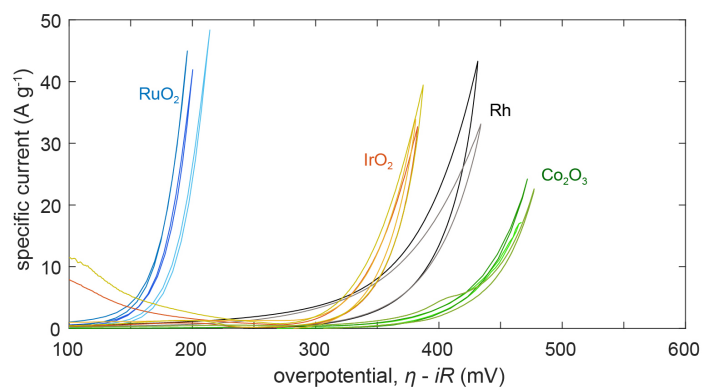


**Fig. S20. Cyclic voltammograms of OER catalysts in 1.0 M H<sub>2</sub>SO<sub>4</sub>.** The scan rate is 2 mV·s<sup>-1</sup>.

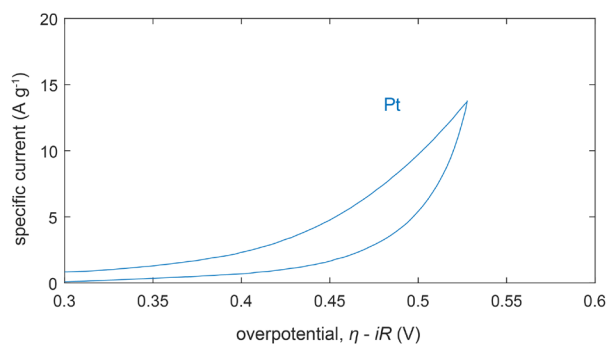


**Fig. S21. Cyclic voltammograms of Pt catalyst for OER in 1.0 M H<sub>2</sub>SO<sub>4</sub>.** The scan rate is 20 mV·s<sup>-1</sup>. For Pt we observed degradation of the acid OER performance after each cycle. We attribute the degradation to oxide formation on the high-surface-area nanoparticle powder, in agreement with previous work (62).

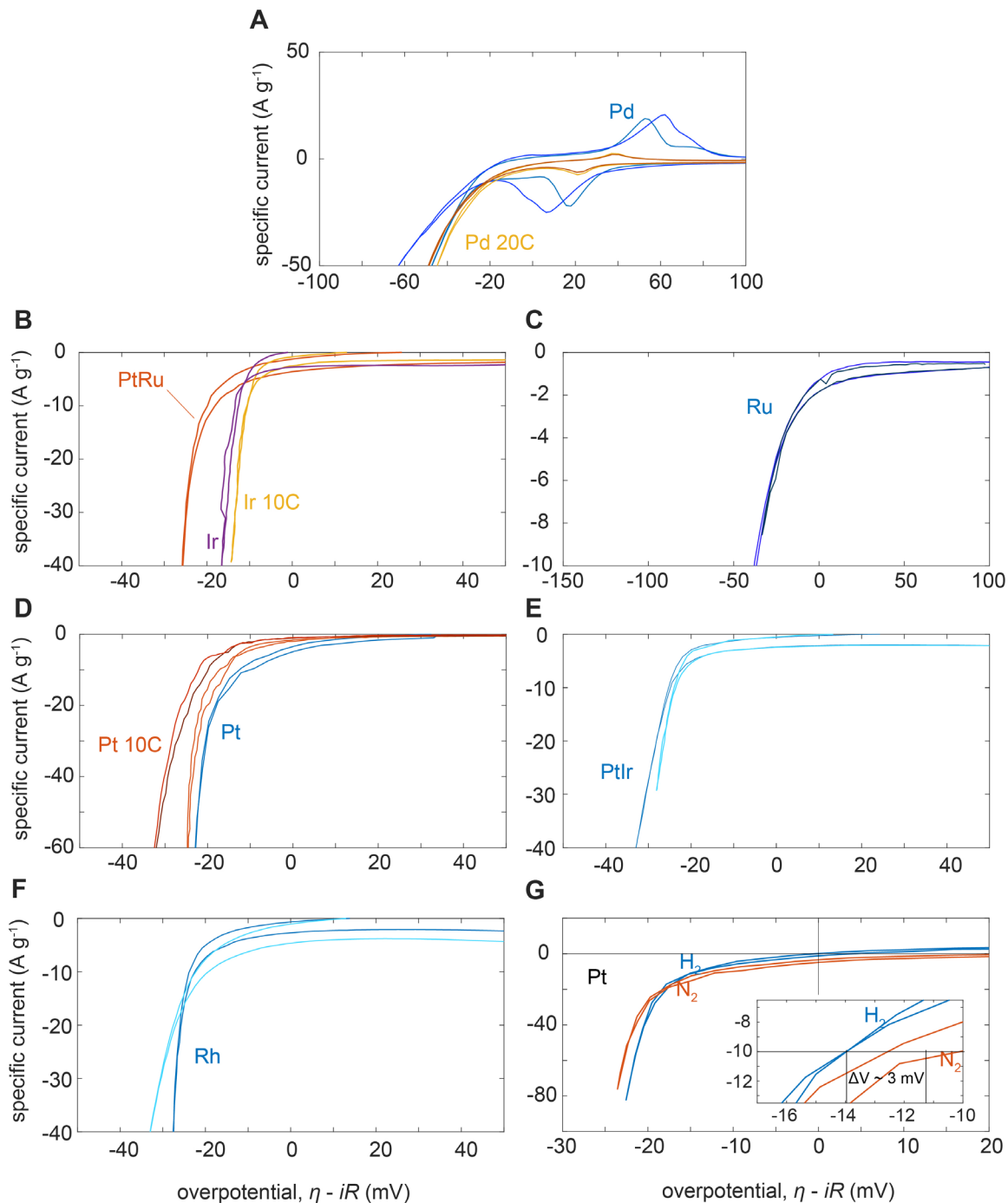


**Fig. S22. Cyclic voltammograms from HER catalysts in 1.0 M H<sub>2</sub>SO<sub>4</sub>.** The scan rate is 2 mV·s<sup>-1</sup>. Panels (A) - (D) show the effect of ALD decoration with TiO<sub>2</sub> (number of ALD cycles indicated by a number followed by the letter C) on the HER performance of various catalysts. All the measurements were performed while bubbling N<sub>2</sub>. To investigate the effect of the local H<sub>2</sub> concentration differing from standard conditions, we also measured a cyclic voltammogram while sparging with H<sub>2</sub> at 1 atm (G). As can be seen, sparging H<sub>2</sub> leads to a marked difference at low current densities due to the absence of the hydrogen oxidation current with N<sub>2</sub> sparging. However, at higher current densities the evolved H<sub>2</sub> at the electrode surface leads to local conditions that are similar to the ones created during H<sub>2</sub> sparging. We note that for the trends observed in Fig. 3, a slight variation in electrocatalytic overpotential by a few mV does not impact the interpretation of the results.

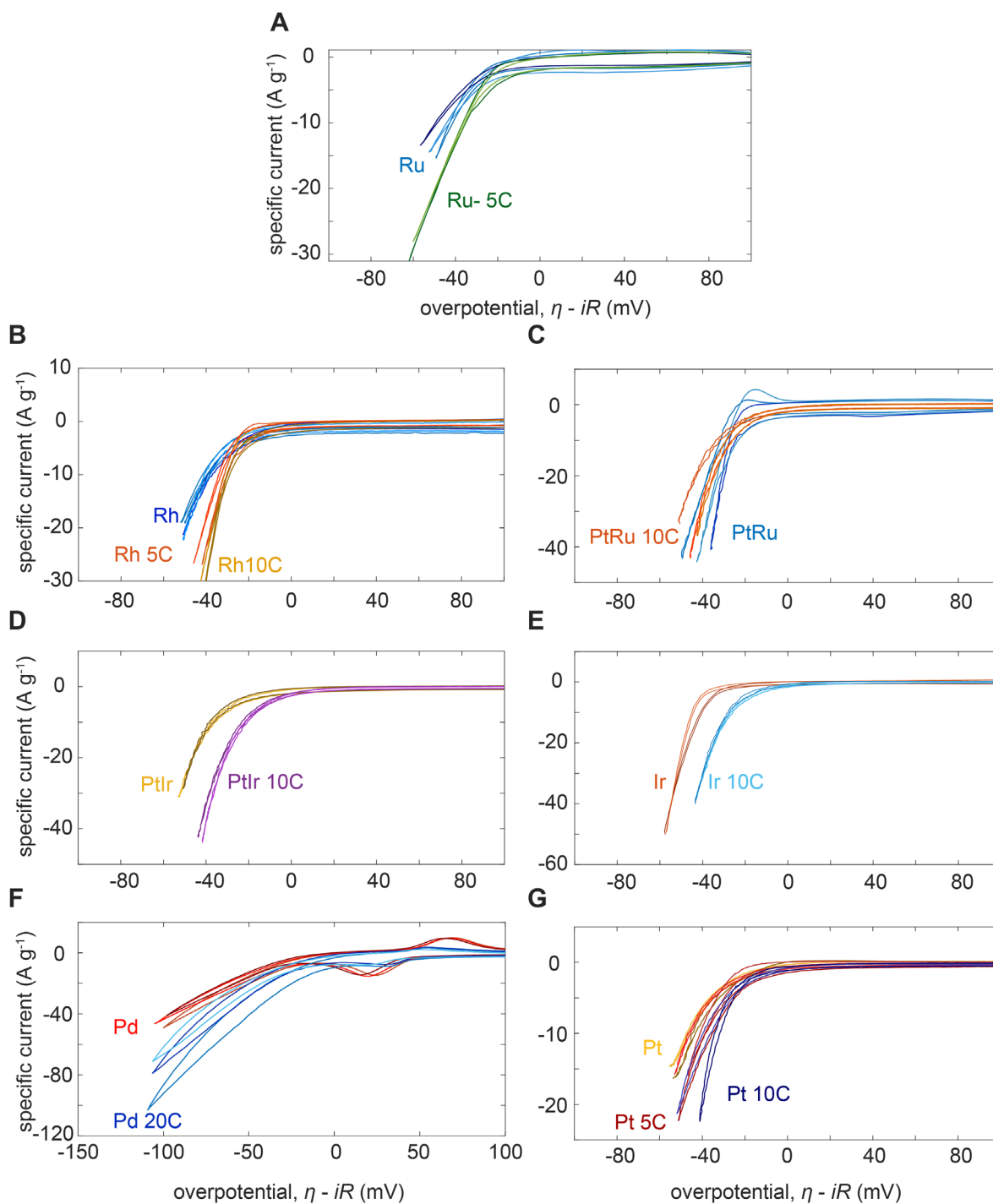


**Fig. S23. Cyclic voltammograms of HER catalysts in 1 M KOH.** The scan rate is 2 mV·s<sup>-1</sup>. Panels (A) - (G) show the effect of ALD decoration with TiO<sub>2</sub> (number of ALD cycles indicated by a number followed by the letter C) on the HER performance of various catalysts. Generally the addition of TiO<sub>2</sub> increases the HER activity.

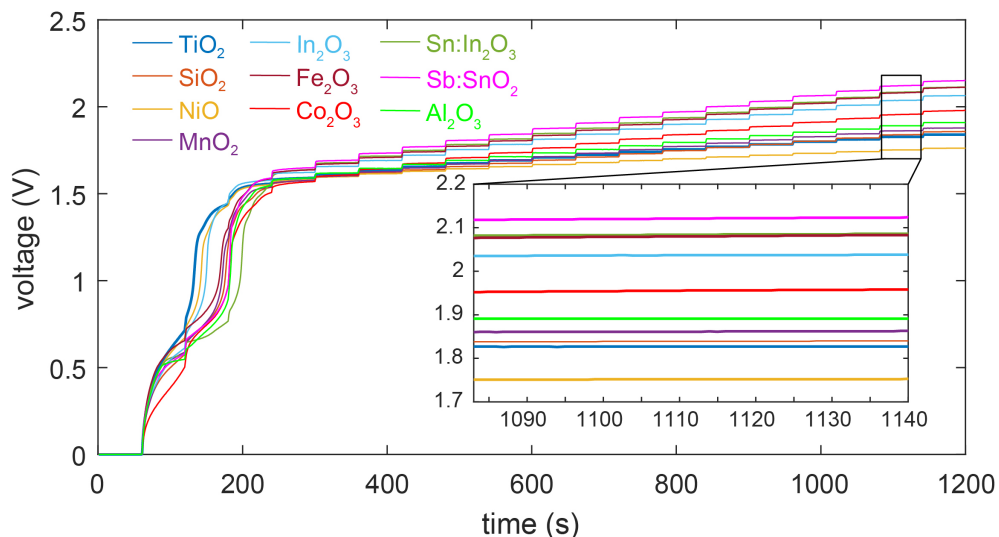


**Fig. S24. Full voltage response as a function of time during current steps for BPM electrolyzers.** Various WD catalysts (as shown in the legend) were used on the basic AEL surface with Sb:SnO<sub>2</sub> on the acidic CEL surface. As can be seen, a time window of 60 s for each 2.5 mA·cm<sup>-2</sup> current density step is sufficient to reach a voltage plateau that allows reliable comparison of different catalyst layers. However, relatively constant degradation rates (~ 2-5 mV/min) are observed throughout different measurements. To investigate if those changes might be a reflection of catalyst dissolution, which could impact our results shown in Fig. 2 and 3, we extracted the degradation rate for each current density step from a 55 s time window (5s after the initial transient voltage change due to the applied current density change) and analyzed as indicated in the below figure. More-detailed stability and degradation studies are needed to fully understand the time response and mechanisms behind the slow performance loss.

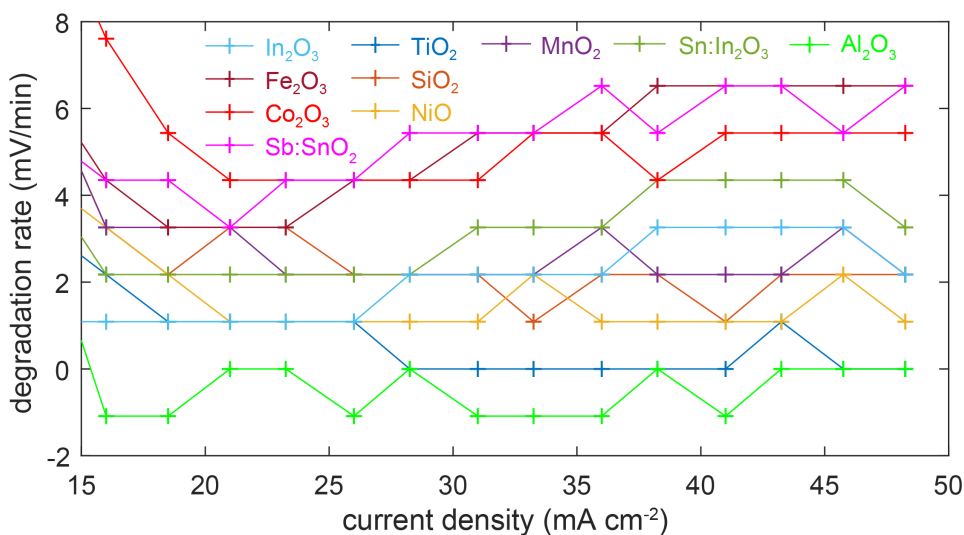


**Fig. S25. Degradation rates at different current-density steps.** Most catalysts show a relatively constant degradation rate throughout the applied current-density range, independent of the measured WD activity. This is evidence that any degradation processes occurring are not linked directly to the measured WD activity.

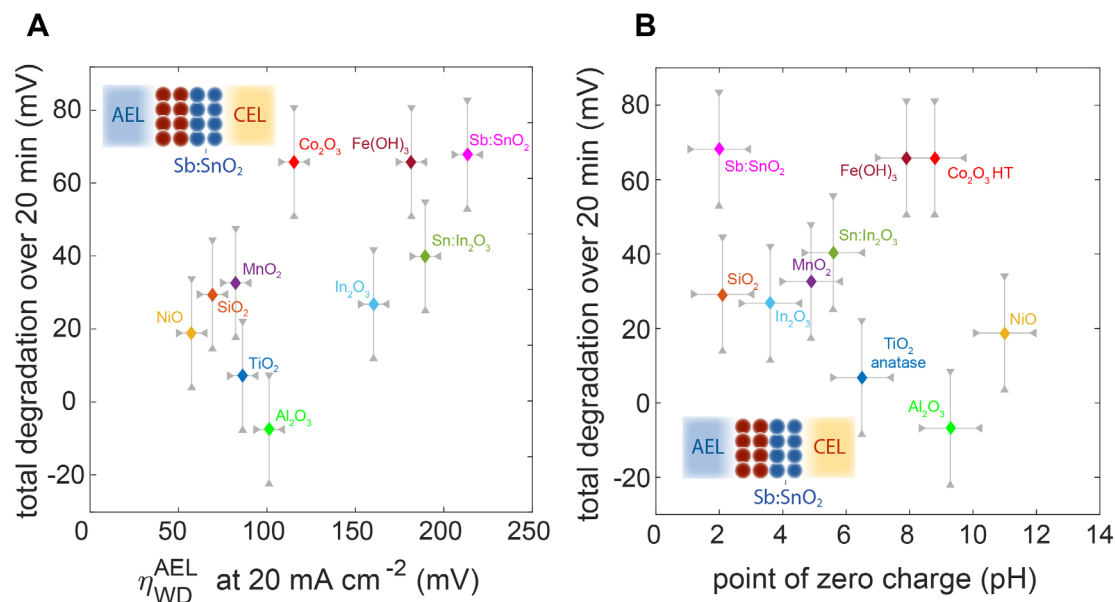


**Fig. S26. Total degradation over a 20-min electrolyzer polarization study versus WD overpotential and PZC for various catalysts on the AEL surface.** The degradation rates shown in Fig. S23 are integrated over all current steps to obtain the values shown here. **(A)** By comparing the total voltage degradation with  $\eta_{wd}$ , we find that catalyst dissolution, and possible currents carried by dissolved ion species other than H<sup>+</sup> and OH<sup>-</sup> lowering the overall measured potential, cannot explain the apparent enhanced WD kinetics in our electrolyzer measurements. **(B)** By comparing the total voltage degradation versus the PZC of the investigated catalysts, we also find no clear correlation of WD-catalyst-dissolution rate with PZC. Catalyst dissolution is therefore unlikely the source of the observed correlation between PZC and  $\eta_{wd}$ . The errors for PZC and  $\eta_{wd}$  are the same as for the data shown in the main manuscript. The range (one standard deviation) of apparent degradation is estimated from three IrO<sub>2</sub> single-layer BPMs.

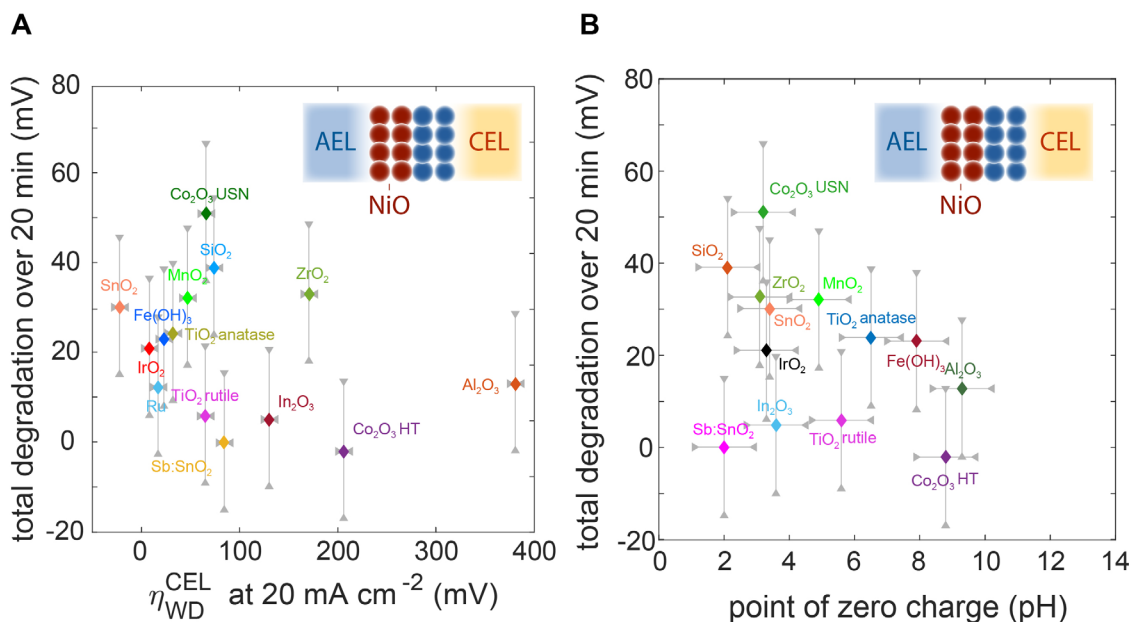


**Fig. S27. Total degradation over a 20-min electrolyzer polarization scan versus  $\eta_{wd}$  and PZC for WD catalysts on the CEL surface.** **(A)** The total degradation observed during the electrolyzer measurements does not correlate with  $\eta_{wd}$ . **(B)** The total degradation does not correlate with the PZC of the investigated WD catalysts. Therefore, the data in Figure 2

is unlikely to be explained by a PZC-dependent catalyst-degradation hypothesis.

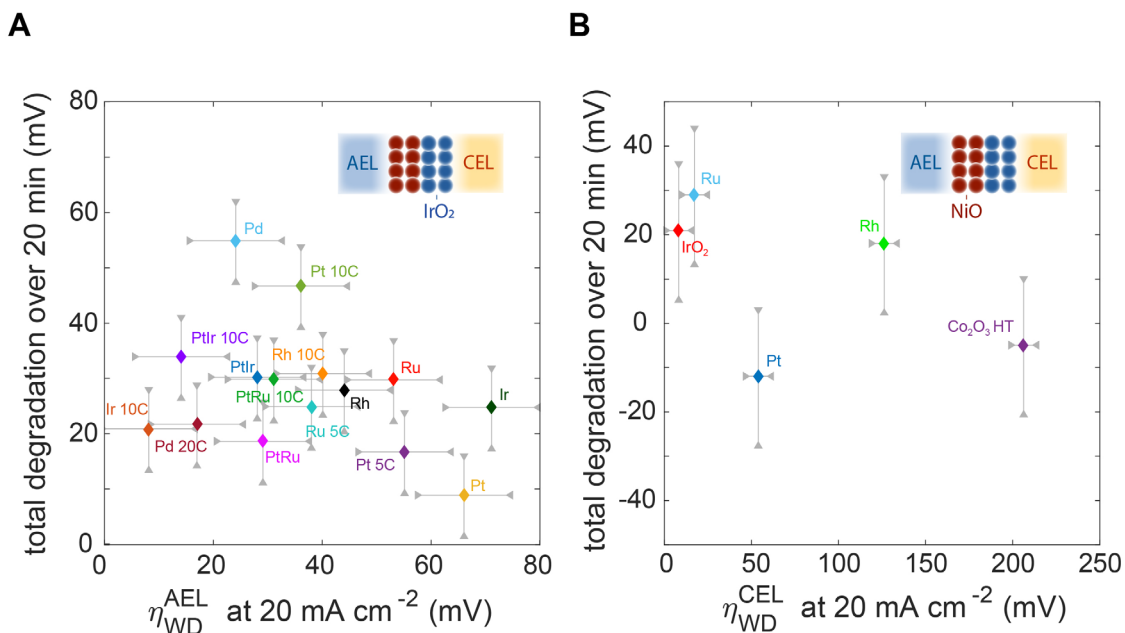


**Fig. S28. Total degradation over a 20-min electrolyzer polarization scan versus  $\eta_{wd}$  for varying base-HER and acid-OER catalysts on the AEL and CEL surface, respectively. (A)** Total degradation versus  $\eta_{wd}$  for varying base HER catalysts on the AEL surface. **(B)** Total degradation versus  $\eta_{wd}$  for varying acid OER catalysts on the CEL surface. The total degradation (or improvement in B) versus  $\eta_{wd}$  for the investigated catalysts does not show any clear correlation that could explain the observed results in Fig. 3 based on a catalyst-degradation hypothesis.

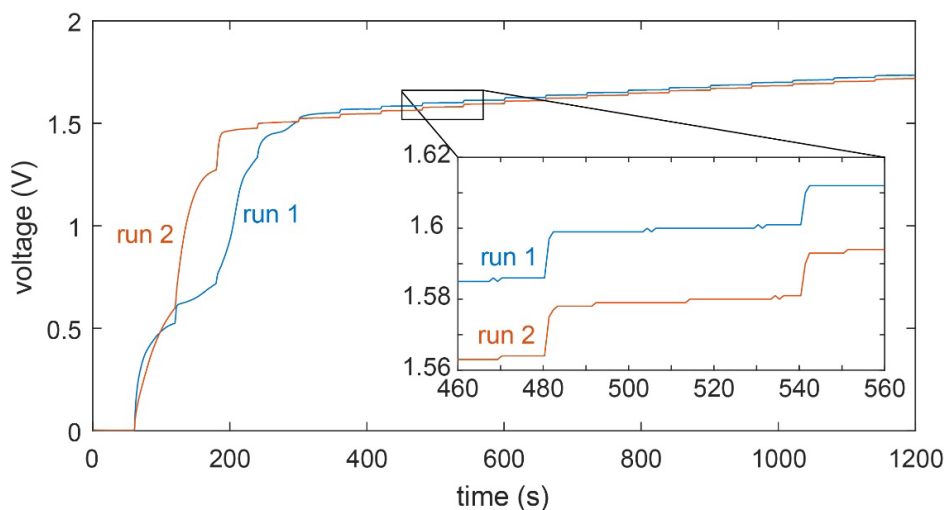


**Fig. S29. Time traces of Ir-TiO<sub>2</sub>/10C(AEL)|IrO<sub>2</sub>(CEL) double-layer BPM electrolyzer for two subsequent BPM-electrolyzer tests.** The current density is stepped in 2.5 mA·cm<sup>-2</sup> increments every 60 s. Although we observe, in general, a slow apparent degradation of the performance during galvanostatic measurements, as shown in Fig. S25-S28, we often observe an overall improvement in performance during the second and subsequent galvanostatic measurements (see also Fig. S30). This might be ascribed to an activation process of the WD, OER, or HER catalysts and/or an improvement of the catalyst/ionomer/membrane interfaces, a common observation for AEM and PEM electrolyzers. However, because the time dependence (i.e. both activation and degradation phenomena) are not fully understood at this point, we only show the first cycle of galvanostatic BPM electrolyzer measurements and use that data for all subsequent

calculation of  $\eta_{\text{wd}}$ . At low current densities, the electrolyzers show voltage transients with current below 1.23V, which we ascribe to the consumption of free acid and base in the system (for details see supplementary discussion above).

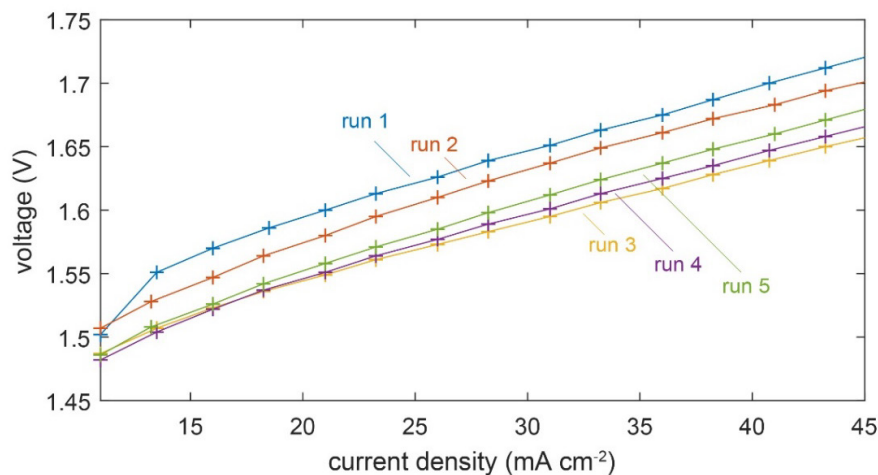


**Fig. S30. Repeated polarization curves of the Ir-TiO<sub>2</sub>/10C(AEL)|IrO<sub>2</sub>(CEL) double-layer BPM electrolyzer.** During repeat measurements many of the double-layer BPMs improve in performance. For example, the total voltage driving electrolysis at 20 mA cm<sup>-2</sup> decreases by ~40 mV between runs 1 and 4, but then slightly increases during run 5. Understanding the activation and long-term degradation processes in these devices (which is likely related to catalyst, ionomer, and interfacial chemical changes) will require further detailed study. For practical BPM applications providing long-term stability, optimized nanoparticle WD catalysts likely need to be embedded into a polymer binder between the two membranes.

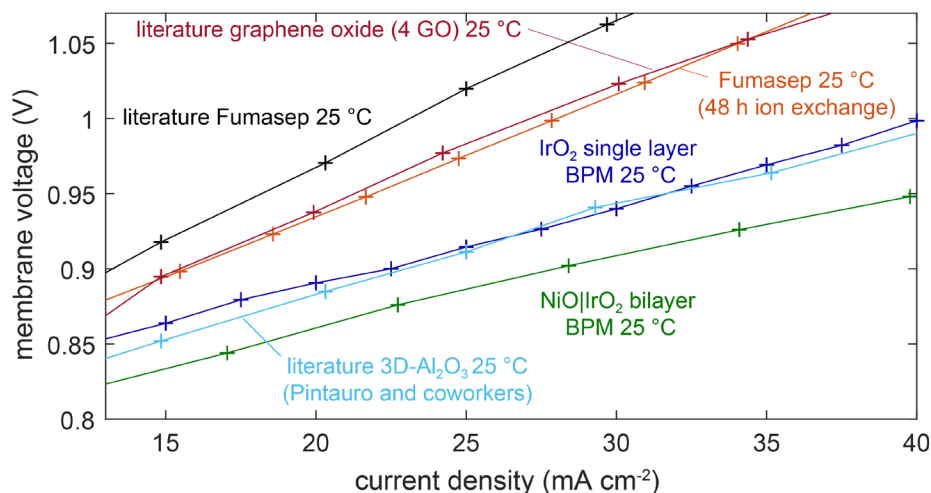


**Fig. S31. Comparison of IrO<sub>2</sub> single-layer and NiO|IrO<sub>2</sub> BPM measured at 25 °C to other literature data.** To compare our BPMs to literature data, we measured single-layer IrO<sub>2</sub> BPMs (dark blue) and NiO|IrO<sub>2</sub> bilayer BPMs (green) at 25 °C in the H-cell and compare the results to the values reported in the literature at similar conditions. We measured our membranes with 1 M acid and base on each side, and the literature values are obtained for 0.5 M acid and base in the two compartments (24). The single-layer IrO<sub>2</sub> BPM data appears better than values reported for a commercial Fumasep FBM (Fumatech) membrane (black) and also custom BPMs with graphene-oxide catalysts (red) substantially at 25 °C. To ensure that the apparently better performance of the single-layer BPMs versus the commercial Fumasep BPMs does not originate from an artefact associated with our measurement setup, we independently characterized a Fumasep BPM. We observed a strong dependence of the BPM performance on the length of the pre-testing ion-exchange process in an H-cell filled with KOH and HCl in the anode and cathode compartment, respectively (Fumasep BPMs are shipped in Cl<sup>-</sup> form). After ~48 h (orange line) we observed the best and stable performance, which however was still inferior to the single-layer IrO<sub>2</sub> BPMs (green and purple) and the literature 3d-Al<sub>2</sub>O<sub>3</sub>-BPM values (blue). The literature 3d-Al<sub>2</sub>O<sub>3</sub> BPMs are on par to our single-layer BPMs, when measured in comparable conditions as in Ref. (24), and as also shown in Table S1. The best double-layer BPMs appear superior (green). We note that different membranes have been used for the 3d-

Al<sub>2</sub>O<sub>3</sub> and the bilayer BPMs reported here, so different co-ion leakage during the H-cell measurements could influence the membrane voltage slightly at 20 mA·cm<sup>-2</sup>.

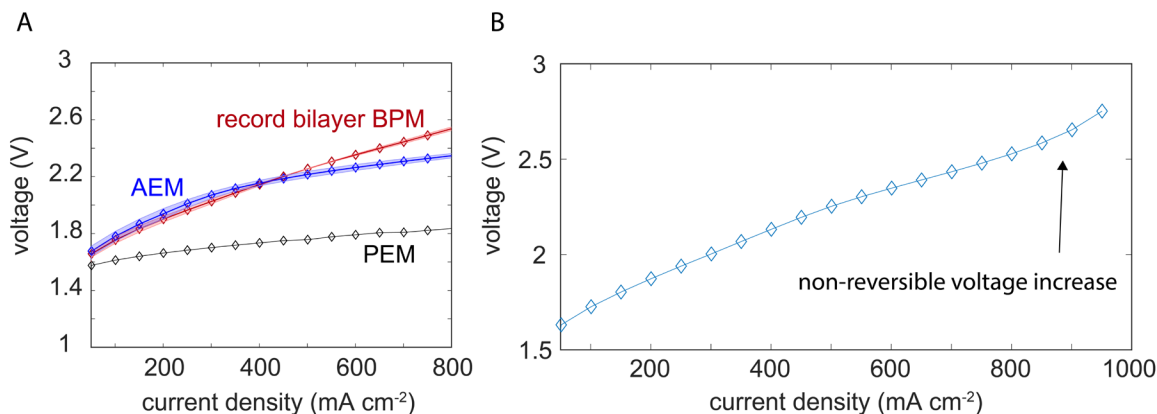


**Fig. S32. Champion bilayer BPM at high current densities.** (A) Comparison of the champion bilayer BPM, reference AEM and PEM electrolyzers. The shaded area shows one standard deviation obtained from three independent measurements. Up to 400 mA·cm<sup>-2</sup>, the AEM and bilayer BPM electrolyzer perform similarly. However, at higher current densities the differential resistance of the AEM electrolyzer is similar to that of the PEM electrolyzer, likely indicating a similar series resistance limitation of the MEAs produced by our fabrication method (which can be improved). However, the BPM electrolyzer voltage increases further. (B) At current densities above 800 mA·cm<sup>-2</sup> we observe a non-reversible voltage increase for the BPM electrolyzers. This non-reversible inflection point in the polarization curve is often ascribed to water transport limitations (63). The BPM junction dries out and the hydration of reactive OH<sup>-</sup> is reduced, which leads to increased degradation of the polymer backbone due to nucleophilic attack. Further study is needed to understand if this limitation also impacts the measured BPM performance at lower current densities and if it can be removed, e.g. by using thinner membranes with better water transport.

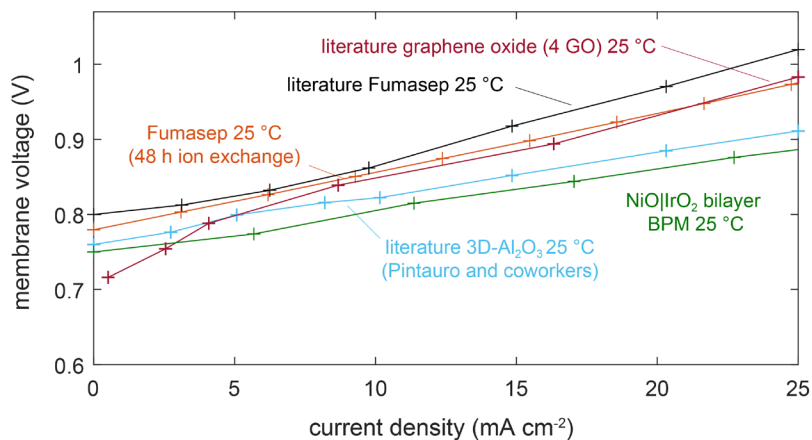


**Fig. S33. Low current-density range of NiO|IrO<sub>2</sub> BPM and other literature values at 25 °C.** At low current density, H-cell measurements are affected by co-ion leakage of secondary electrolyte ions across the BPM leading to a parasitic, charge-compensating current. We measured our membranes with 1 M acid and base on each side, and the literature values are obtained for 0.5 M acid and base in the two compartments (24). As can be seen, the BPMs reported here are similar to those in the literature and show a lower open-circuit potential than expected from theoretical considerations. At high current densities this leakage current becomes negligible which also motivates the choice of 20 mA·cm<sup>-2</sup> to report  $\eta_{wd}$ . The propensity for counter-ion-leakage is related to the ion-selectivity of the membranes and thus is not a focus of this study. The electrolyzer measurements are not affected by this complication and all virtually all current is due to water dissociation due to the lack of substantial free counter ions.

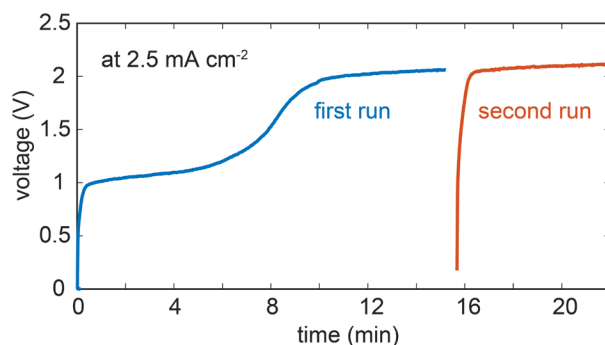


**Fig. S34. Voltage transients at low current density ( $2.5 \text{ mA}\cdot\text{cm}^{-2}$ ) for two subsequent BPM-electrolyzer tests without WD catalyst.** The current density is held constant at  $2.5 \text{ mA}\cdot\text{cm}^{-2}$ . For the first run (blue), keeping the low current density constant for 10 min shows that after initial apparent stabilization (4 min) the voltage increases again until reaching its final value  $\sim 2 \text{ V}$ . The second run (orange) does not exhibit this behavior, indicating the initial behavior is likely correlated with the consumption of some species other than water (e.g. free acid and base). Due to this effect, we do not show the low voltage behavior in the electrolyzer polarization curves, which were collected by stepping the current in  $2.5 \text{ mA}\cdot\text{cm}^{-2}$  increments for 60 s each. As this reference BPM does not contain any WD-catalyst particles, the effect is unrelated to the catalyst particles.

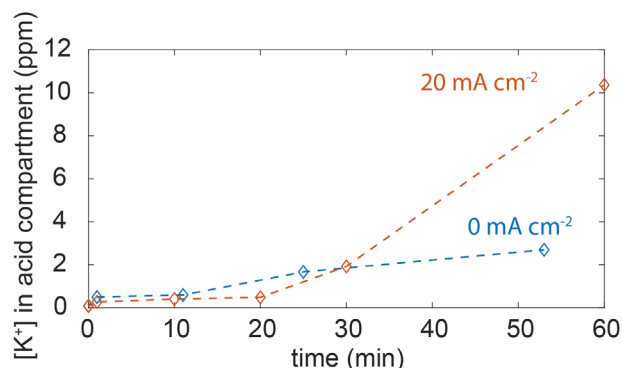


**Fig. S35.  $\text{K}^+$  crossover from alkaline anode compartment through AEL and CEL and into the acidic cathode compartment, measured by ICP-MS.** Due to non-ideal permselectivity of the AEL,  $\text{K}^+$  crosses through the AEL, then ion-exchanges in the CEL and eventually enters the acidic cathode compartment. At open circuit,  $0 \text{ mA}\cdot\text{cm}^{-2}$ , the  $[\text{K}^+]$  in the acid compartment increases steadily, driven by the chemical potential gradient of the  $\text{K}^+$  between the alkaline and acidic compartments. At  $20 \text{ mA}\cdot\text{cm}^{-2}$  for the first 20 min only a small increase in  $[\text{K}^+]$  is detectable, similar to the increase at open circuit. Afterwards,  $[\text{K}^+]$  increases faster. Taking the crossover rate between 30 and 60 min ( $5 \text{ ppb s}^{-1}$ ) at a total current of 80 mA (surface area  $4 \text{ cm}^2$ ) and a total volume of 80 ml of the acid compartment, a total current due to  $\text{K}^+$  crossover of  $\sim 1 \text{ mA}$  is found. Therefore, at  $20 \text{ mA}\cdot\text{cm}^{-2}$  the current is mainly carried by  $\text{H}^+$  and  $\text{OH}^-$  originating from WD and only less than 2% is due to leakage current through the H-cell. The  $\eta_{\text{wd}}$  determined in the H-cell to calibrate the MEA setup are thus a close approximation to the true  $\eta_{\text{wd}}$ .

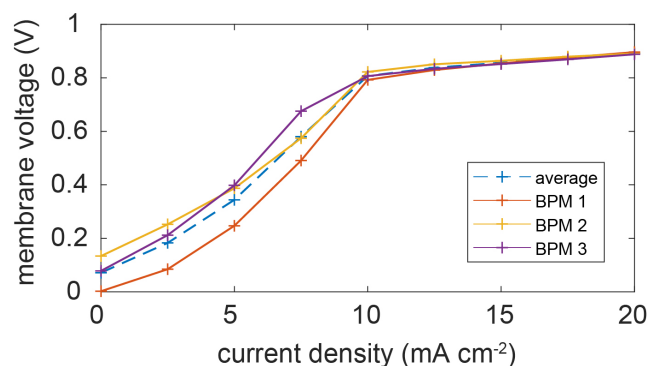


**Fig. S36. Polarization curves at low current densities of three single-layer IrO<sub>2</sub> BPMs measured in an H-cell.** The behavior at low current densities is influenced by the degree of ion-exchange during the pretreatment of the membranes, any preconditioning, and the leakage current due to co-ion crossover (see Fig. S35). The measured membrane voltage is below the ideal Nernstian value of ~ 814 mV (at 20 °C) for the current density range below ~ 10 mA·cm<sup>-2</sup> during the first polarization run. Although substantial leakage current is expected at low current densities, at 20 mA·cm<sup>-2</sup> only a small fraction (< 2 %) of the total current is due to this co-ion conduction (as shown by ICP-MS in Fig. S35) and the main current is carried by H<sup>+</sup> and OH<sup>-</sup>. Notably, the large spread between different samples with the same WD catalyst layer at low current densities vanish at higher current densities, further confirming that all the membranes reach the same steady-state condition at 20 mA·cm<sup>-2</sup> where nearly all the current is associated with WD and further supporting the use of 20 mA·cm<sup>-2</sup> to measure  $\eta_{wd}$ .

**Table S1. Overview of research and commercial BPMs.\***

$\eta_{wd}$ (mV) est. at 20 mA·cm <sup>-2</sup>	T (°C)	Electrolyte(s)	WD catalyst, (AEL CEL)	# layers, geometry	CEL	AEL	year	ref.
?	?	?	ion exchange Ti, Ru, Sn, Pd, Zr-cations	1,2D	Neosepta CM-1	aminated PS	1991	(15)
?	?	?	Fe(OH) <sub>3</sub> , Co(OH) <sub>2</sub> , Ni(OH) <sub>2</sub>	1,2D	?	?	1994	(64)
11,400	25	NaCl	S-PEEK 2.1	1, 2D	S-PEEK/PES	A-PSF	2010	(12)
5,770	25	NaCl	S-PEEK 2.1+2 wt% Fe(OH) <sub>3</sub> (sol gel)	1, 2D	S-PEEK/PES	A-PSF	2010	(12)
4,870	25	NaCl	S-PEEK 2.1+poly(ferrocenyl dimethylsilane)	1, 2D	S-PEEK/PES	A-PSF	2010	(12)
4,670	30	NaCl	Ti(O) <sub>x</sub> (H) <sub>y</sub>	1, 2D	PES	chloromethylated and aminated PS	2012	(14)
3,620	25	NaCl	S-PEEK 2.1	1, 2D	S-PEEK/PES	Pall R4030	2010	(12)
3,370	30	NaCl	Zr(O) <sub>x</sub> (H) <sub>y</sub>	1, 2D	PES	chloromethylated and aminated PS	2012	(14)
2,670	30	NaCl	Si(O) <sub>x</sub> (H) <sub>y</sub>	1, 2D	PES	chloromethylated/ and aminated PS	2012	(14)
1,750-2,470	25	Na <sub>2</sub> SO <sub>4</sub>	Fe-MIL-101-NH <sub>2</sub>	1,2D	SPPO	QPPO	2017	(66)
1,470	30	NaCl	PEG-3400	1, 2D	N-methylene phosphonic chitosan	quaternized chitosan	2011	(67)
590-920	25	Na <sub>2</sub> SO <sub>4</sub>	bovine serum albumin	1,2D	SPPO	QA/3362BW	2004	(68)
75-870	25	Na <sub>2</sub> SO <sub>4</sub>	PAMAM with Cr(III)	1,2D	SPPO	QA/3362BW	2006	(69)
0-1,350	25	Na <sub>2</sub> SO <sub>4</sub>	PVA	1,2D	SPPO	QA	2005	(70)
520	25	NaCl	S-PEEK 2.1+80 nm poly(4-vinylpyridine)	1, 2D	S-PEEK/PES	A-Psf (Fumatech)	2010	(12)
320	25	Na <sub>2</sub> SO <sub>4</sub>	Boltron	1, 2D	SPPO	3362 BW (QA)	2007	(71)
108	25	KOH H <sub>2</sub> SO <sub>4</sub>	graphene oxide	1, 2D	Nafion	Neosepta AHA (Tokuyama)	2018	(24)
167	25	NaClO <sub>4</sub>	graphene oxide	1, 2D	Nafion	Neosepta AHA (Tokuyama)	2014	(72)

105	25	KOH H <sub>2</sub> SO <sub>4</sub>	Fumasep BPM (Fumatech)	?, 2D	-	-	2019	This work
140	25	KOH H <sub>2</sub> SO <sub>4</sub>	Fumasep BPM (Fumatech)	?, 2D	-	-	2018	(24)
100	25	NaCl	PEDOT:PSS/PEI	3,2D	SPEEK	FAA3 (Fumatech)	2013	(25)
70	25	NaCl/NaOH	Neosepta (Tokuyama)	?, 2D	-	-	2007	(65)
~ 0	25	0.5 M Na <sub>2</sub> SO <sub>4</sub>	Al <sub>2</sub> O <sub>3</sub>	1, 3D	SPEEK	QPPO	2017	(11)
~ 50	25	KOH H <sub>2</sub> SO <sub>4</sub>	Al <sub>2</sub> O <sub>3</sub>	1, 3D	SPEEK	QPPO	2018	(24)
0 - 381	50	KOH H <sub>2</sub> SO <sub>4</sub> /di-H <sub>2</sub> O	43 metal oxide combi.	2, 2D	Nafion	Sustainion (Dioxide Materials)	2019	this work
381	50	di-H <sub>2</sub> O	NiO (AEL)  Al <sub>2</sub> O <sub>3</sub> (CEL)	2, 2D	Nafion	Sustainion	2019	''
60 ± 9	25	KOH H <sub>2</sub> SO <sub>4</sub>	IrO <sub>2</sub>	1, 2D	Nafion	Sustainion	2019	''
44 ± 9	50	KOH H <sub>2</sub> SO <sub>4</sub> /di-H <sub>2</sub> O	IrO <sub>2</sub>	1, 2D	Nafion	Sustainion	2019	''
32 ± 9	50	di-H <sub>2</sub> O	NiO (AEL) TiO <sub>2</sub> (CEL)	2, 2D	Nafion	Sustainion	2019	''
29 ± 9	50	di-H <sub>2</sub> O	PtRu (AEL) IrO <sub>2</sub> (CEL)	2, 2D	Nafion	Sustainion	2019	''
29 ± 9	50	di-H <sub>2</sub> O	NiO (AEL) SnO <sub>2</sub> (CEL)	2, 2D	Nafion	Sustainion	2019	''
28 ± 9	50	di-H <sub>2</sub> O	PtIr (AEL) IrO <sub>2</sub> (CEL)	2, 2D	Nafion	Sustainion	2019	''
24 ± 9	50	di-H <sub>2</sub> O	Pd (AEL) IrO <sub>2</sub> (CEL)	2, 2D	Nafion	Sustainion	2019	''
23 ± 9	50	di-H <sub>2</sub> O	NiO (AEL) Fe(OH) <sub>3</sub> (CEL)	2, 2D	Nafion	Sustainion	2019	''
17 ± 9	50	di-H <sub>2</sub> O	NiO (AEL) RuO <sub>2</sub> (CEL)	2, 2D	Nafion	Sustainion	2019	''
17 ± 9	50	di-H <sub>2</sub> O	Pd/20c (AEL) IrO <sub>2</sub> (CEL)	2, 2D	Nafion	Sustainion	2019	''
14 ± 9	50	di-H <sub>2</sub> O	PtIr/10C (AEL) IrO <sub>2</sub> (CEL)	2, 2D	Nafion	Sustainion	2019	''
8 ± 9	50	di-H <sub>2</sub> O	NiO (AEL) IrO <sub>2</sub> (CEL)	2, 2D	Nafion	Sustainion	2019	''
8 ± 9	50	di-H <sub>2</sub> O	Ir/10C (AEL) IrO <sub>2</sub> (CEL)	2, 2D	Nafion	Sustainion	2019	''

\* The employed WD catalyst inside the BPM junction is usually limited to one layer for the different studies with few exceptions, including this study. The BPM junction geometry is approximately planar, i.e. 2D, for all studies except the work by Pintauro and coworkers (11). WD can also be driven at the membrane end groups / surfaces facing the junction, and therefore the employed AELs and CELs are listed. We note that the  $\eta_{wd}$  aggregated in this table from literature sources were *estimated* from the measurements of the electrostatic potential across the membrane in an H-cell configuration. However, because neutral (unbuffered) salt solutions were typically used on either side of the AEL and CEL, the BPM was not generating acid/base under standard conditions and therefore the effective equilibrium membrane potential is unknown and likely changing with time. It is possible that the values are underestimations of the true  $\eta_{wd}$ . Our studies avoid this issue by using reference H-cell measurements with 1.0 M acid and base electrolytes.

Table S2. Properties of nanoparticles WD catalysts\*

material	size (nm)	source	Experimental PZC (pH)	Literature PZC/IEP (pH), Ref. (73)
IrO <sub>2</sub>	5-10	FCS	3.3	< 2 - 3.3
RuO <sub>2</sub>	5-10	FCS	(2-3) not reliable	2.8 - 6.1
Pt	5-7.5	FCS	inert	
Ir	4-6	FCS	inert	
PtRu	3-5	FCS	inert	
PtIr	4-6	FCS	inert	
Pd	15	USN	inert	
Rh	15	USN	inert	
Ru	15	USN	inert	
TiO <sub>2</sub> - rutile	30	USN	5.6	1.9 - 6.8
TiO <sub>2</sub> - anatase	30	USN	6.5	1.7 - 6.8
SiO <sub>2</sub>	20	NCX	2.1	1 - 7.1
Co <sub>2</sub> O <sub>3</sub> -USN	50	USN	3.2	2.2 - 11.4 (including other oxidation states)
Co <sub>2</sub> O <sub>3</sub> -HT	50-100	HT	8.8	2.2 - 11.4 (including other oxidation states)
NiO	15-35	USN	11	3.5-12.7
MnO <sub>2</sub>	40	USN	4.9	2 - 10 (including other oxidation states)
ZrO <sub>2</sub>	40	USN	3.1	3.5 - 9.5
SnO <sub>2</sub>	35-55	USN	3.4	< 2 - 7
Al <sub>2</sub> O <sub>3</sub>	50	USN	9.3	3.6 - 11.4
Sb:SnO <sub>2</sub>	50	USN	2	< 1 - 3.7
Sn:In <sub>2</sub> O <sub>3</sub>	20-70	USN	3.5	2.5 - 8.5
In <sub>2</sub> O <sub>3</sub>	20-70	USN	3.6	5.4 - 9
Fe(OH) <sub>3</sub>	10	USN	7.9	4.5 - 8

\*As-received/as-synthesized nanoparticle catalysts and their properties as quoted by the vendor (size) or measured (PZC). The abbreviations of the sources are; **FCS**: Fuel Cell Store, **USN**: US Research Nanomaterials, **NCX**: Nanocomposix, **HT**: self-made *via* hydrothermal methods. PZC values reported in the literature vary widely across a large range depending on the exact material (crystal phase, stoichiometry etc.) and especially the synthesis method. Therefore, we use the PZCs measured in our laboratory for all materials studied.

## References and Notes

1. T. Luo, S. Abdu, M. Wessling, Selectivity of ion exchange membranes: A review. *J. Membr. Sci.* **555**, 429–454 (2018). [doi:10.1016/j.memsci.2018.03.051](https://doi.org/10.1016/j.memsci.2018.03.051)
2. R. S. Reiter, W. White, S. Ardo, Electrochemical characterization of commercial bipolar membranes under electrolyte conditions relevant to solar fuels technologies. *J. Electrochem. Soc.* **163**, H3132–H3134 (2016). [doi:10.1149/2.0201604jes](https://doi.org/10.1149/2.0201604jes)
3. Y. Tanaka, *Ion Exchange Membranes: Fundamentals and Applications* (Elsevier, 2007).
4. D. A. Vermaas, M. Sassenburg, W. A. Smith, Photo-assisted water splitting with bipolar membrane induced pH gradients for practical solar fuel devices. *J. Mater. Chem. A Mater. Energy Sustain.* **3**, 19556–19562 (2015). [doi:10.1039/C5TA06315A](https://doi.org/10.1039/C5TA06315A)
5. Y. C. Li, D. Zhou, Z. Yan, R. H. Gonçalves, D. A. Salvatore, C. P. Berlinguette, T. E. Mallouk, Electrolysis of CO<sub>2</sub> to syngas in bipolar membrane-based electrochemical cells. *ACS Energy Lett.* **1**, 1149–1153 (2016). [doi:10.1021/acsenergylett.6b00475](https://doi.org/10.1021/acsenergylett.6b00475)
6. D. A. Vermaas, W. A. Smith, Synergistic electrochemical CO<sub>2</sub> reduction and water oxidation with a bipolar membrane. *ACS Energy Lett.* **1**, 1143–1148 (2016). [doi:10.1021/acsenergylett.6b00557](https://doi.org/10.1021/acsenergylett.6b00557)
7. Y. C. Li, Z. Yan, J. Hitt, R. Wycisk, P. N. Pintauro, T. E. Mallouk, Bipolar membranes inhibit product crossover in CO<sub>2</sub> electrolysis cells. *Adv. Sustainable Syst.* **2**, 1700187 (2018). [doi:10.1002/adsu.201700187](https://doi.org/10.1002/adsu.201700187)
8. M. Lin, L. Han, M. R. Singh, C. Xiang, An experimental- and simulation-based evaluation of the CO<sub>2</sub> utilization efficiency of aqueous-based electrochemical CO<sub>2</sub> reduction reactors with ion-selective membranes. *ACS Appl. Energy Mater.* **2**, 5843–5850 (2019). [doi:10.1021/acsaem.9b00986](https://doi.org/10.1021/acsaem.9b00986)
9. Y. C. Li, G. Lee, T. Yuan, Y. Wang, D.-H. Nam, Z. Wang, F. P. García de Arquer, Y. Lum, C.-T. Dinh, O. Voznyy, E. H. Sargent, CO<sub>2</sub> electroreduction from carbonate electrolyte. *ACS Energy Lett.* **4**, 1427–1431 (2019). [doi:10.1021/acsenergylett.9b00975](https://doi.org/10.1021/acsenergylett.9b00975)
10. J. M. Ahlfield, L. Liu, P. A. Kohl, PEM/AEM junction design for bipolar membrane fuel cells. *J. Electrochem. Soc.* **164**, F1165–F1171 (2017). [doi:10.1149/2.1041712jes](https://doi.org/10.1149/2.1041712jes)
11. C. H. Shen, R. Wycisk, P. N. Pintauro, High performance electrospun bipolar membrane with a 3D junction. *Energy Environ. Sci.* **10**, 1435–1442 (2017). [doi:10.1039/C7EE00345E](https://doi.org/10.1039/C7EE00345E)
12. J. Balster, S. Srinantharajah, R. Sumbharaju, I. Pünt, R. G. H. Lammertink, D. F. Stamatialis, M. Wessling, Tailoring the interface layer of the bipolar membrane. *J. Membr. Sci.* **365**, 389–398 (2010). [doi:10.1016/j.memsci.2010.09.034](https://doi.org/10.1016/j.memsci.2010.09.034)
13. S. S. Mel'nikov, O. V. Shapovalova, N. V. Shel'deshov, V. I. Zabolotskii, Effect of d-metal hydroxides on water dissociation in bipolar membranes. *Petrol. Chem.* **51**, 577–584 (2011). [doi:10.1134/S0965544111070097](https://doi.org/10.1134/S0965544111070097)
14. A. M. Rajesh, T. Chakrabarty, S. Prakash, V. K. Shahi, Effects of metal alkoxides on electro-assisted water dissociation across bipolar membranes. *Electrochim. Acta* **66**, 325–331 (2012). [doi:10.1016/j.electacta.2012.01.102](https://doi.org/10.1016/j.electacta.2012.01.102)

15. F. Hanada, K. Hiraya, N. Ohmura, S. Tanaka, Bipolar membrane and method for its production. European Patent EP0459820B1 (1991).
16. Y. Oda, T. Yawataya, Neutrality-disturbance phenomenon of membrane-solution systems. *Desalination* **5**, 129–138 (1968). [doi:10.1016/S0011-9164\(00\)80208-8](https://doi.org/10.1016/S0011-9164(00)80208-8)
17. M.-S. Kang, Y.-J. Choi, H.-J. Lee, S.-H. Moon, Effects of inorganic substances on water splitting in ion-exchange membranes. I. Electrochemical characteristics of ion-exchange membranes coated with iron hydroxide/oxide and silica sol. *J. Colloid Interface Sci.* **273**, 523–532 (2004). [doi:10.1016/j.jcis.2004.01.050](https://doi.org/10.1016/j.jcis.2004.01.050) [Medline](#)
18. R. Simons, Strong electric field effects on proton transfer between membrane-bound amines and water. *Nature* **280**, 824–826 (1979). [doi:10.1038/280824a0](https://doi.org/10.1038/280824a0)
19. R. Simons, G. Khanarian, Water dissociation in bipolar membranes: Experiments and theory. *J. Membr. Biol.* **38**, 11–30 (1978). [doi:10.1007/BF01875160](https://doi.org/10.1007/BF01875160)
20. H. Strathmann, H. J. Rapp, B. Bauer, C. M. Bell, Theoretical and practical aspects of preparing bipolar membranes. *Desalination* **90**, 303–323 (1993). [doi:10.1016/0011-9164\(93\)80183-N](https://doi.org/10.1016/0011-9164(93)80183-N)
21. A. B. Yaroslavtsev, V. V. Nikonenko, V. I. Zabolotsky, Ion transfer in ion-exchange and membrane materials. *Russ. Chem. Rev.* **72**, 393–421 (2003). [doi:10.1070/RC2003v072n05ABEH000797](https://doi.org/10.1070/RC2003v072n05ABEH000797)
22. V. I. Zabolotskii, N. V. Shel'deshov, N. P. Gnusin, Dissociation of water molecules in systems with ion-exchange membranes. *Russ. Chem. Rev.* **57**, 801–808 (1988). [doi:10.1070/RC1988v057n08ABEH003389](https://doi.org/10.1070/RC1988v057n08ABEH003389)
23. A. J. B. Kemperman, *Handbook on Bipolar Membrane Technology* (Twente Univ. Press, 2000).
24. Z. Yan, L. Zhu, Y. C. Li, R. J. Wycisk, P. N. Pintauro, M. A. Hickner, T. E. Mallouk, The balance of electric field and interfacial catalysis in promoting water dissociation in bipolar membranes. *Energy Environ. Sci.* **11**, 2235–2245 (2018). [doi:10.1039/C8EE01192C](https://doi.org/10.1039/C8EE01192C)
25. S. Abdu, K. Sricharoen, J. E. Wong, E. S. Muljadi, T. Melin, M. Wessling, Catalytic polyelectrolyte multilayers at the bipolar membrane interface. *ACS Appl. Mater. Interfaces* **5**, 10445–10455 (2013). [doi:10.1021/am403019y](https://doi.org/10.1021/am403019y) [Medline](#)
26. M. Moqadam, A. Lervik, E. Riccardi, V. Venkatraman, B. K. Alsberg, T. S. van Erp, Local initiation conditions for water autoionization. *Proc. Natl. Acad. Sci. U.S.A.* **115**, E4569–E4576 (2018). [doi:10.1073/pnas.1714070115](https://doi.org/10.1073/pnas.1714070115) [Medline](#)
27. M. Eigen, L. d. Maeyer, Untersuchungen über die kinetik der neutralization. *Z. Elektrochem.* **59**, 986 (1955).
28. G. Ertl, H. Gerischer, Ein vergleich der kinetik der neutralisationsreaktionen des leichten und schweren wassers. *Z. Elektrochem.* **66**, 560 (1962).
29. C. V. Ovesen, P. Stoltze, J. K. Nørskov, C. T. Campbell, A kinetic model of the water gas shift reaction. *J. Catal.* **134**, 445–468 (1992). [doi:10.1016/0021-9517\(92\)90334-E](https://doi.org/10.1016/0021-9517(92)90334-E)

30. M. Sterrer, N. Nilius, S. Shaikhutdinov, M. Heyde, T. Schmidt, H.-J. Freund, Interaction of water with oxide thin film model systems. *J. Mater. Res.* **34**, 360–378 (2019). [doi:10.1557/jmr.2018.454](https://doi.org/10.1557/jmr.2018.454)
31. P. A. Thiel, T. E. Madey, The interaction of water with solid surfaces: Fundamental aspects. *Surf. Sci. Rep.* **7**, 211–385 (1987). [doi:10.1016/0167-5729\(87\)90001-X](https://doi.org/10.1016/0167-5729(87)90001-X)
32. I. Bertini, C. Luchinat, “The reaction pathways of zinc enzymes and related biological catalysts,” in *Bioinorganic Chemistry* (University Science Books, 1994), pp. 37–106.
33. D. Xu, M. B. Stevens, M. R. Cosby, S. Z. Oener, A. M. Smith, L. J. Enman, K. E. Ayers, C. B. Capuano, J. N. Renner, N. Danilovic, Y. Li, H. Wang, Q. Zhang, S. W. Boettcher, Earth-abundant oxygen electrocatalysts for alkaline anion-exchange-membrane water electrolysis: Effects of catalyst conductivity and comparison with performance in three-electrode cells. *ACS Catal.* **9**, 7–15 (2019). [doi:10.1021/acscatal.8b04001](https://doi.org/10.1021/acscatal.8b04001)
34. N. Danilovic, R. Subbaraman, D. Strmcnik, K.-C. Chang, A. P. Paulikas, V. R. Stamenkovic, N. M. Markovic, Enhancing the alkaline hydrogen evolution reaction activity through the bifunctionality of Ni(OH)<sub>2</sub>/metal catalysts. *Angew. Chem. Int. Ed.* **51**, 12495–12498 (2012). [doi:10.1002/anie.201204842](https://doi.org/10.1002/anie.201204842) [Medline](#)
35. R. Subbaraman, D. Tripkovic, D. Strmcnik, K. C. Chang, M. Uchimura, A. P. Paulikas, V. Stamenkovic, N. M. Markovic, Enhancing hydrogen evolution activity in water splitting by tailoring Li<sup>+</sup>-Ni(OH)<sub>2</sub>-Pt interfaces. *Science* **334**, 1256–1260 (2011). [doi:10.1126/science.1211934](https://doi.org/10.1126/science.1211934) [Medline](#)
36. X. Chen, I. T. McCrum, K. A. Schwarz, M. J. Janik, M. T. M. Koper, Co-adsorption of cations as the cause of the apparent pH dependence of hydrogen adsorption on a stepped platinum single-crystal electrode. *Angew. Chem. Int. Ed.* **56**, 15025–15029 (2017). [doi:10.1002/anie.201709455](https://doi.org/10.1002/anie.201709455) [Medline](#)
37. I. Ledezma-Yanez, W. D. Z. Wallace, P. Sebastián-Pascual, V. Climent, J. M. Feliu, M. T. M. Koper, Interfacial water reorganization as a pH-dependent descriptor of the hydrogen evolution rate on platinum electrodes. *Nat. Energy* **2**, 17031 (2017). [doi:10.1038/nenergy.2017.31](https://doi.org/10.1038/nenergy.2017.31)
38. J. Zheng, W. Sheng, Z. Zhuang, B. Xu, Y. Yan, Universal dependence of hydrogen oxidation and evolution reaction activity of platinum-group metals on pH and hydrogen binding energy. *Sci. Adv.* **2**, e1501602 (2016). [doi:10.1126/sciadv.1501602](https://doi.org/10.1126/sciadv.1501602) [Medline](#)
39. M. Luo, Z. Wang, Y. C. Li, J. Li, F. Li, Y. Lum, D.-H. Nam, B. Chen, J. Wicks, A. Xu, T. Zhuang, W. R. Leow, X. Wang, C.-T. Dinh, Y. Wang, Y. Wang, D. Sinton, E. H. Sargent, Hydroxide promotes carbon dioxide electroreduction to ethanol on copper via tuning of adsorbed hydrogen. *Nat. Commun.* **10**, 5814 (2019). [doi:10.1038/s41467-019-13833-8](https://doi.org/10.1038/s41467-019-13833-8) [Medline](#)
40. S. Z. Oener, S. Ardo, S. W. Boettcher, Ionic processes in water electrolysis: The role of ion-selective membranes. *ACS Energy Lett.* **2**, 2625–2634 (2017). [doi:10.1021/acsenergylett.7b00764](https://doi.org/10.1021/acsenergylett.7b00764)
41. J. N. Mills, I. T. McCrum, M. J. Janik, Alkali cation specific adsorption onto fcc(111) transition metal electrodes. *Phys. Chem. Chem. Phys.* **16**, 13699–13707 (2014). [doi:10.1039/C4CP00760C](https://doi.org/10.1039/C4CP00760C) [Medline](#)

42. E. Liu, J. Li, L. Jiao, H. T. T. Doan, Z. Liu, Z. Zhao, Y. Huang, K. M. Abraham, S. Mukerjee, Q. Jia, Unifying the hydrogen evolution and oxidation reactions kinetics in base by identifying the catalytic roles of hydroxyl-water-cation adducts. *J. Am. Chem. Soc.* **141**, 3232–3239 (2019). [doi:10.1021/jacs.8b13228](https://doi.org/10.1021/jacs.8b13228) [Medline](#)
43. H. P. Boehm, Acidic and basic properties of hydroxylated metal oxide surfaces. *Discuss. Faraday Soc.* **52**, 264–275 (1971). [doi:10.1039/df9715200264](https://doi.org/10.1039/df9715200264)
44. D. S. Smith, F. G. Ferris, Proton binding by hydrous ferric oxide and aluminum oxide surfaces interpreted using fully optimized continuous pKa spectra. *Environ. Sci. Technol.* **35**, 4637–4642 (2001). [doi:10.1021/es0018668](https://doi.org/10.1021/es0018668) [Medline](#)
45. X. Liu, J. Cheng, X. Lu, R. Wang, Surface acidity of quartz: Understanding the crystallographic control. *Phys. Chem. Chem. Phys.* **16**, 26909–26916 (2014). [doi:10.1039/C4CP02955K](https://doi.org/10.1039/C4CP02955K) [Medline](#)
46. M. K. Ridley, V. A. Hackley, M. L. Machesky, Characterization and surface-reactivity of nanocrystalline anatase in aqueous solutions. *Langmuir* **22**, 10972–10982 (2006). [doi:10.1021/la061774h](https://doi.org/10.1021/la061774h) [Medline](#)
47. L. Onsager, Deviations from Ohm's law in weak electrolytes. *J. Chem. Phys.* **2**, 599–615 (1934). [doi:10.1063/1.1749541](https://doi.org/10.1063/1.1749541)
48. M. A. Blommaert, D. A. Vermaas, B. Izelaar, B. in 't Veen, W. A. Smith, Electrochemical impedance spectroscopy as a performance indicator of water dissociation in bipolar membranes. *J. Mater. Chem. A Mater. Energy Sustain.* **7**, 19060–19069 (2019). [doi:10.1039/C9TA04592A](https://doi.org/10.1039/C9TA04592A)
49. H. Strathmann, J. J. Krol, H. J. Rapp, G. Eigenberger, Limiting current density and water dissociation in bipolar membranes. *J. Membr. Sci.* **125**, 123–142 (1997). [doi:10.1016/S0376-7388\(96\)00185-8](https://doi.org/10.1016/S0376-7388(96)00185-8)
50. I. C. Man, H.-Y. Su, F. Calle-Vallejo, H. A. Hansen, J. I. Martínez, N. G. Inoglu, J. Kitchin, T. F. Jaramillo, J. K. Nørskov, J. Rossmeisl, Universality in oxygen evolution electrocatalysis on oxide surfaces. *ChemCatChem* **3**, 1159–1165 (2011). [doi:10.1002/cctc.201000397](https://doi.org/10.1002/cctc.201000397)
51. M. Pourbaix, *Atlas of Electrochemical Equilibria in Aqueous Solutions* (National Association of Corrosion, 1974).
52. M. B. McDonald, S. Ardo, N. S. Lewis, M. S. Freund, Use of bipolar membranes for maintaining steady-state pH gradients in membrane-supported, solar-driven water splitting. *ChemSusChem* **7**, 3021–3027 (2014). [doi:10.1002/cssc.201402288](https://doi.org/10.1002/cssc.201402288) [Medline](#)
53. M. Park, E. S. Beh, E. M. Fell, Y. Jing, E. F. Kerr, D. Porcellinis, M.-A. Goulet, J. Ryu, A. A. Wong, R. G. Gordon, J. Cho, M. J. Aziz, A high voltage aqueous zinc–organic hybrid flow battery. *Adv. Energy Mater.* **9**, 1900694 (2019). [doi:10.1002/aenm.201900694](https://doi.org/10.1002/aenm.201900694)
54. J. Xia, G. Eigenberger, H. Strathmann, U. Niekem, Flow battery based on reverse electrodialysis with bipolar membranes: Single cell experiments. *J. Membr. Sci.* **565**, 157–168 (2018). [doi:10.1016/j.memsci.2018.07.073](https://doi.org/10.1016/j.memsci.2018.07.073)

55. S. Z. Oener, M. J. Foster, S. W. Boettcher, Tabulated data for: Accelerating water dissociation in bipolar membranes and for electrocatalysis. Zenodo (2020); <https://doi.org/10.5281/zenodo.3897673>.
56. W. Zhao, M. Bajdich, S. Carey, A. Vojvodic, J. K. Nørskov, C. T. Campbell, Water dissociative adsorption on NiO(111): Energetics and structure of the hydroxylated surface. *ACS Catal.* **6**, 7377–7384 (2016). [doi:10.1021/acscatal.6b01997](https://doi.org/10.1021/acscatal.6b01997)
57. H. Ali, R. Seidel, A. Bergmann, B. Winter, Electronic structure of aqueous-phase anatase titanium dioxide nanoparticles probed by liquid jet photoelectron spectroscopy. *J. Mater. Chem. A Mater. Energy Sustain.* **7**, 6665–6675 (2019). [doi:10.1039/C8TA09414D](https://doi.org/10.1039/C8TA09414D)
58. K. N. Grew, J. P. McClure, D. Chu, P. A. Kohl, J. M. Ahlfield, Understanding transport at the acid- alkaline interface of bipolar membranes. *J. Electrochem. Soc.* **163**, F1572–F1587 (2016). [doi:10.1149/2.0941614jes](https://doi.org/10.1149/2.0941614jes)
59. F. G. Wilhelm, I. Pünt, N. F. A. van der Vegt, H. Strathmann, M. Wessling, Asymmetric bipolar membranes in acid–base electro dialysis. *Ind. Eng. Chem. Res.* **41**, 579–586 (2002). [doi:10.1021/ie010524n](https://doi.org/10.1021/ie010524n)
60. M. A. Henderson, The interaction of water with solid surfaces: Fundamental aspects revisited. *Surf. Sci. Rep.* **46**, 1–308 (2002). [doi:10.1016/S0167-5729\(01\)00020-6](https://doi.org/10.1016/S0167-5729(01)00020-6)
61. I. T. McCrum, M. J. Janik, pH and alkali cation effects on the Pt cyclic voltammogram explained using density functional theory. *J. Phys. Chem. C* **120**, 457–471 (2016). [doi:10.1021/acs.jpcc.5b10979](https://doi.org/10.1021/acs.jpcc.5b10979)
62. T. Reier, M. Oezaslan, P. Strasser, Electrocatalytic oxygen evolution reaction (OER) on Ru, Ir, and Pt catalysts: A comparative study of nanoparticles and bulk materials. *ACS Catal.* **2**, 1765–1772 (2012). [doi:10.1021/cs3003098](https://doi.org/10.1021/cs3003098)
63. J. J. Krol, M. Jansink, M. Wessling, H. Strathmann, Behaviour of bipolar membranes at high current density: Water diffusion limitation. *Separ. Purif. Tech.* **14**, 41–52 (1998). [doi:10.1016/S1383-5866\(98\)00058-6](https://doi.org/10.1016/S1383-5866(98)00058-6)
64. N. V. Shel'deshov, V. I. Zabolotskii, V. V. Ganych, The effect of insoluble metal hydroxides on the reaction rate of water dissociation on a cation-exchange membrane. *Elektrokhimiya* **30**, 1458–1461 (1994).
65. J. Balster, R. Sumbharaju, S. Srikantharajah, I. Punt, D. F. Stamatialis, V. Jordan, M. Wessling, Asymmetric bipolar membrane: A tool to improve product purity. *J. Membr. Sci.* **287**, 246–256 (2007). [doi:10.1016/j.memsci.2006.10.042](https://doi.org/10.1016/j.memsci.2006.10.042)
66. Q. Y. Wang, B. Wu, C. X. Jiang, Y. M. Wang, T. W. Xu, Improving the water dissociation efficiency in a bipolar membrane with amino-functionalized MIL-101. *J. Membr. Sci.* **524**, 370–376 (2017). [doi:10.1016/j.memsci.2016.11.056](https://doi.org/10.1016/j.memsci.2016.11.056)
67. A. M. Rajesh, M. Kumar, V. K. Shahi, Functionalized biopolymer based bipolar membrane with poly ethylene glycol interfacial layer for improved water splitting. *J. Membr. Sci.* **372**, 249–257 (2011). [doi:10.1016/j.memsci.2011.02.009](https://doi.org/10.1016/j.memsci.2011.02.009)
68. R. Q. Fu, T. W. Xu, W. H. Yang, Z. X. Pan, Fundamental studies on the intermediate layer of a bipolar membrane. Part II. Effect of bovine serum albumin (BSA) on water dissociation

- at the interface of a bipolar membrane. *J. Colloid Interface Sci.* **278**, 318–324 (2004).  
[Medline](#)
69. R. Q. Fu, Y. Y. Cheng, T. W. Xu, W. H. Yang, Fundamental studies on the intermediate layer of a bipolar membrane. Part VI. Effect of the coordinated complex between starburst dendrimer PAMAM and chromium (III) on water dissociation at the interface of a bipolar membrane. *Desalination* **196**, 260–265 (2006). [doi:10.1016/j.desal.2006.03.009](https://doi.org/10.1016/j.desal.2006.03.009)
70. R.-Q. Fu, Y.-H. Xue, T.-W. Xu, W.-H. Yang, Fundamental studies on the intermediate layer of a bipolar membrane part IV. Effect of polyvinyl alcohol (PVA) on water dissociation at the interface of a bipolar membrane. *J. Colloid Interface Sci.* **285**, 281–287 (2005).  
[doi:10.1016/j.jcis.2004.11.050](https://doi.org/10.1016/j.jcis.2004.11.050) [Medline](#)
71. Y. Xue, T. Xu, R. Fu, Y. Cheng, W. Yang, Catalytic water dissociation using hyperbranched aliphatic polyester (Boltorn series) as the interface of a bipolar membrane. *J. Colloid Interface Sci.* **316**, 604–611 (2007). [doi:10.1016/j.jcis.2007.08.052](https://doi.org/10.1016/j.jcis.2007.08.052) [Medline](#)
72. M. B. McDonald, M. S. Freund, Graphene oxide as a water dissociation catalyst in the bipolar membrane interfacial layer. *ACS Appl. Mater. Interfaces* **6**, 13790–13797 (2014).  
[doi:10.1021/am503242y](https://doi.org/10.1021/am503242y) [Medline](#)
73. M. Kosmulski, *Surface Charging and Points of Zero Charge* (CRC, 2009).